Experimental Case Studies for Uncertainty Quantification in Structural Dynamics: Part 2, Plate Experiment

S. Adhikari [a,*,1]

[a] School of Engineering, University of Wales Swansea, Singleton Park, Swansea SA2 8PP, United Kingdom

M. I. Friswell [b,2]

[b] Department of Aerospace Engineering, University of Bristol Queens Building, University Walk, Bristol BS8 1TR, United Kingdom

K. Lonkar [c,3]

[c] Department of Aerospace Engineering, Indian Institute of Technology, Kanpur, India

A. Sarkar [d,4]

[d] Department of Civil Engineering Carleton University, Ottawa, Canada

Abstract

Uncertainty quantification is becoming an integral part in model validation of complex engineering structures. In the companion paper [1] an experiment with 12 masses placed at random locations on a fixed-fixed beam is described with the objective of quantifying uncertainty in a simple dynamical model. From the modeling point of view, this experiment simulates random mass distribution. In this paper an experiment involving a cantilever plate with 10 randomly placed spring-mass oscillators. The oscillating mass of each of the 10 oscillators about 1% of the mass of the plate. This experiment is aimed at simulating the problem of 'unmodelled dynamics', which in turn results in randomness in both mass and stiffness matrices. One hundred nominally identical dynamical systems are created and individually tested. The probabilistic characteristics of the frequency response functions are discussed in the low, medium and high frequency ranges. The variability in the amplitude and phase of the measured frequency response functions is compared with numerical Monte Carlo simulation results. The data obtained here may be useful for the validation of uncertainty quantification and propagation methods in structural dynamics.

Key words: Experimental modal analysis, stochastic dynamical systems, uncertainty quantification, model validation, unmodelled dynamics, plate experiment.

Contents

1 Introduction

In the modelling of complex dynamical systems for engineering applications, high-resolution finite element models are generally adopted as predictive tools for reliable numerical simulations. The ensuing large scale linear system is tackled using domain decomposition methods (substructuring). The implicit assumption inherent to such approach is that the constitutive properties, geometric configurations and boundary conditions in the underlying boundary value problem is prescribed with sufficient accuracy. An analyst attempts to eliminate the primary source of error in the numerical approximation due to the discretization errors by increasing spatial mesh resolution and decreasing the stepsize in the time marching scheme.

In practice however the predictions even from such high resolution numerical models may sometimes exhibit significant differences with the results from physical experiments. Such discrepancy, in part, arises from the uncertainty in the data and model itself adopted for numerical representation of the boundary value problem. When substantial statistical information exists, the theory of probability and stochastic processes offer a rich mathematical

* Corresponding author, Tel: + 44 (0)1792 602088, Fax: + 44 (0)1792 295676

 Email addresses: S.Adhikari@swansea.ac.uk (S. Adhikari), M.I.Friswell@bristol.ac.uk (M. I. Friswell), kuldeepl@iitk.ac.in (K. Lonkar), abhijit_sarkar@carleton.ca (A. Sarkar).

 URLs: http://engweb.swan.ac.uk/∼adhikaris (S. Adhikari),
http://www.aer.bris.ac.uk/contact/academic/friswell/home_page.html (M. I. Friswell),
http://home.iitk.ac.in/∼kuldeepl/ (K. Lonkar), http://www.abhijitsarkar.net/ (A. Sarkar).

[1] Chair of Aerospace Engineering
[2] Sir George White Professor
[3] Student
[4] Assistant Professor and Canada Research Chair

framework to represent such uncertainties. In a probabilistic setting, the data uncertainty associated with the system parameters such as the geometric properties and constitutive relations (i.e. Young's modulus, mass density, Poisson's ratio, damping coefficients etc.) can be modeled as random variables or stochastic processes using the so-called *parametric approach*. Numerous uncertainty analysis techniques are reported in the literatures to propagate the data uncertainty through numerical models, or example, using the stochastic finite element method [2–10]. The companion paper addressed this issue experimentally where one hundred realizations of a beam with random mass distribution is created and tested. Recently, the uncertainty due to modeling error has received attention as this is crucial for model validation [11–19]. The model uncertainty poses serious challenges as the parameters contributing to modeling errors are not available *a priori* and therefore precludes the application of parametric approach to address such issues.

In modelling complex engineering structures such as ships, submarines and helicopter, the lack of complete knowledge of the system contributes to model uncertainty. The substructures attached to the primary structures may contribute to the modeling uncertainty significantly influencing the dynamics of the system in the mid- and high-frequency regimes. In many cases, the dynamical characteristic of subsystems such the cargo, piping, fuel, control cables, electronics and avionics systems in typical marine and aerospace vehicles may be known with sufficient accuracy. Therefore, such systems may not be practicable to conventional finite element modelling in a reliable manner. In general, such modeling uncertainty arising from the subsystems may stem from, but not limited to: (a) incomplete and imprecise constitutive and geometric properties, (b) the lack knowledge of the existence of the subsystems, (c) imprecise locations of their attachment points with the primary structures and their coupling characteristics, (d) incompatible physical laws and geometric scales which govern the dynamics of the subsystems demanding multiphysics and multiscale modeling.

The dynamics of the subsystem may be adequately modelled by a set of added-masses to investigate the low frequency (modal) response of the structures. In the mid-frequency range however sprung-mass model of the subsystems is required for accurate estimation of the frequency response functions, the latter being significant to capture the wave-propagation effects. Adhikari and Sarkar [20] conducted an numerical investigation to study the effect of model uncertainty emerging from a set of randomly distributed sprung-masses attached to a homogeneous thin plate. In this paper the issue of modeling uncertainty is investigated experimentally. The scarce experimental studies on random system conducted so far [21–23] do not explicitly consider model-form uncertainty. This is perhaps the first serious attempt to consider modeling uncertainty experimentally. The experiments reported here attempt to simulate the influence of *uncertain* secondary systems on the dynamics of a thin plate (i.e. the

primary structure). A cantilever steel plate with 10 spring-mass oscillators is considered. The spatial attachment locations and the natural frequencies of the sprung-mass oscillators are assumed to be random. The tests are closely controlled and the uncertainty can be considered to be 'known' for all practical purposes. This allows one to model uncertainty, propagate it through dynamical models and compare the results with this experimentally obtained data. One hundred nominally identical dynamical systems are created and individually tested in the Bristol Laboratory for Advanced Dynamic Engineering (BLADE). The model of the cantilever plate and experimental setup are described in section 2. The experimental method to test one hundred nominally identical structures are discussed in section 3. In section 4 the probabilistic characteristics of the amplitude and phase of the measured frequency response functions are discussed in the low, medium and high frequency ranges. In section 5 the experimental system with random mass distribution is numerically simulated using the thin plate theory and Monte Carlo simulation. In section 6 the mean and standard deviation of the amplitude and phase of the experimentally measured frequency response functions are compared with Monte Carlo simulation results. The key results and the contributions of this work are discussed in section 7. The data presented here are available on the world wide web for research purposes. The web address is http://engweb.swan.ac.uk/∼adhikaris/uq/. This data may be used as a benchmark dataset to validate different uncertainty quantification, propagation and model validation methods in structural dynamics and other theoretical developments.

2   System Model and Experimental Setup

The aim of this experiment is to simulate uncertain unmodelled dynamics. The uncertain dynamics is realized by 10 spring-mass oscillators with randomly distributed stiffness properties attached at random locations. This test rig, like the previous experiment described in the companion paper [1], has been designed for simplicity and ease of replication and modelling. The overall arrangement of the test-rig is shown in Figure 1. rectangular steel plate with uniform thickness is used for the experiment. The physical and geometrical properties of the steel plate are shown in Table 1. The plate is clamped along one edge using a clamping device. The clamping device is attached on the top of a heavy concrete block and the whole assembly is placed on a steel table. The plate has a mass of approximately 12.47 kg and special care has been taken to ensure its stability and to minimize vibration transmission. The plate is 'divided' into 375 elements (25 along the length and 15 along the width). Taking one corner of the cantilevered edge as the origin, co-ordinates have been assigned to all of the nodes. Oscillators and accelerometers are attached to these nodes. This approach allows easy correlation to a finite element model, where the oscillators are attached and the measurements are made

Plate Properties	Numerical values
Length (L_x)	998 mm
Width (L_y)	530 mm
Thickness (t_h)	3.0 mm
Mass density (ρ)	7860 kg/m^3
Young's modulus (E)	2.0×10^5 MPa
Poissons ratio (μ)	0.3
Total weight	12.47 kg

Table 1
Material and geometric properties of the cantilever plate considered for the experiment

Oscillator Number	Spring stiffness $(\times 10^4$ N/m)	Natural Frequency (Hz)
1	1.6800	59.2060
2	0.9100	43.5744
3	1.7030	59.6099
4	2.4000	70.7647
5	1.5670	57.1801
6	2.2880	69.0938
7	1.7030	59.6099
8	2.2880	69.0938
9	2.1360	66.7592
10	1.9800	64.2752

Table 2
 Stiffness of the springs and natural frequency of the oscillators used to simulate unmodelled dynamics (the mass of the each oscillator is 121.4g).
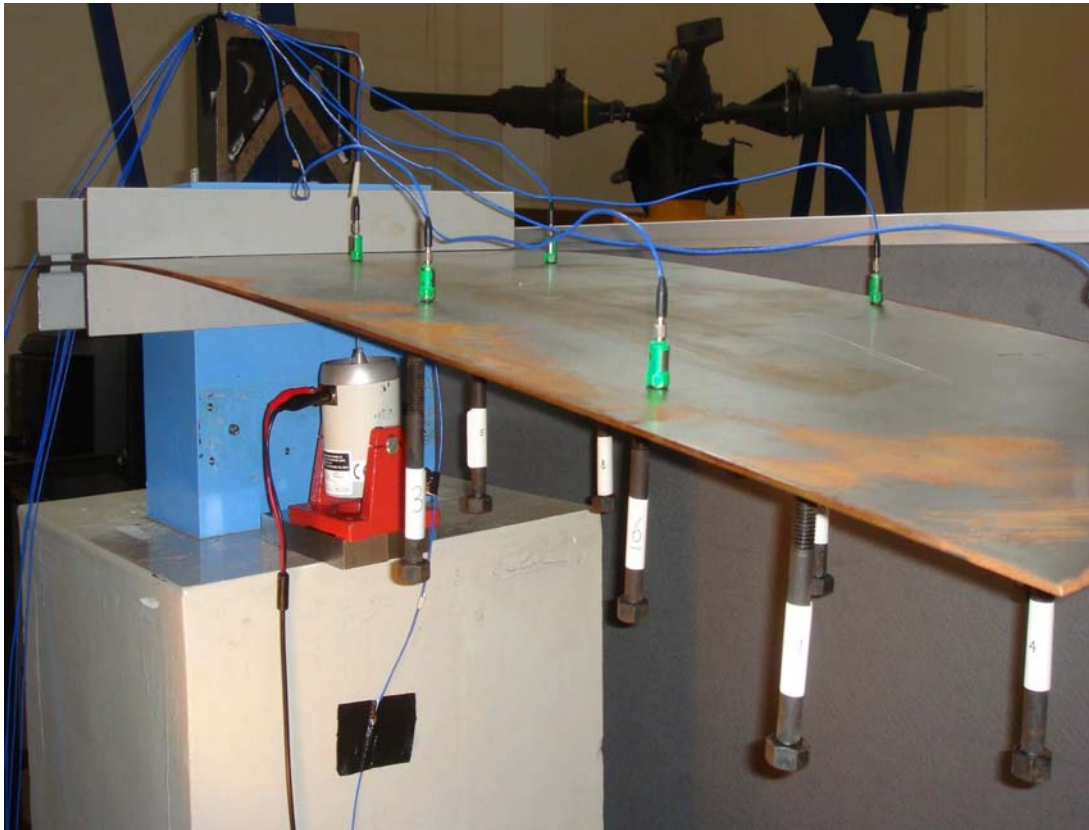
(a) Front view of the experimental setup

(b) Side view of the experimental setup

Fig. 1. The test rig for the cantilever beam plate.
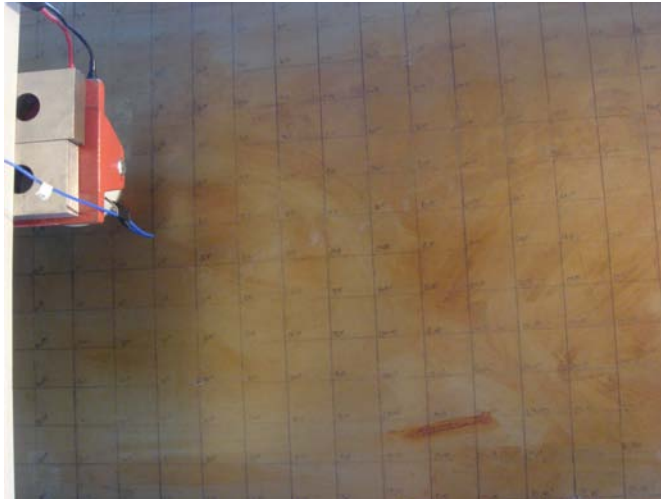
Fig. 2. Grid numbering strategy on the bottom surface of the plate to attach the oscillators.

Fig. 3. Details of a typical oscillator used to simulate unmodelled dynamics. Fixed mass (magnet) 2g, oscillatory mass (the nut) 121.4g. The oscillatory mass is about 1% of the total mass of the plate. The spring stiffness varies between 1.5 and 2.4 $\times 10^4$ N/m.

Fig. 4. Attached oscillators at random locations. The spring stiffness varies so that the oscillator frequencies are between 43 and 70 Hz.
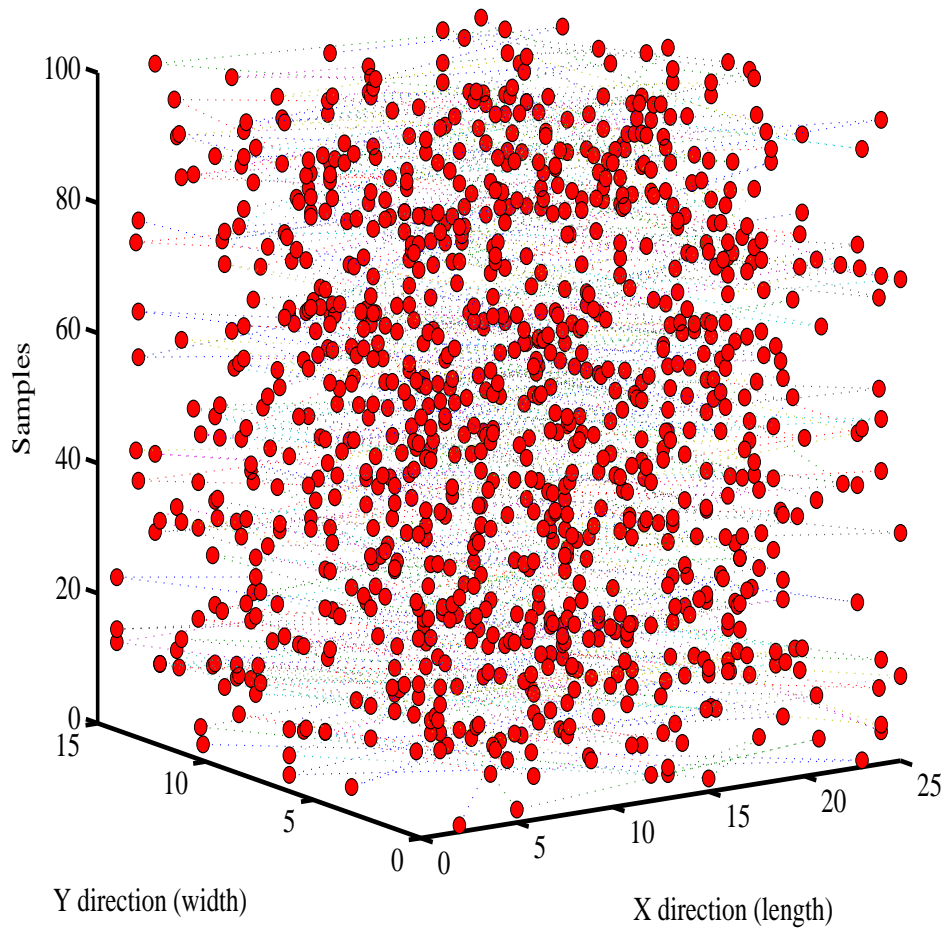
Fig. 5. All 100 samples of the locations of the 10 oscillators along the length of the beam. The sample number is shown in the Z-axis. For each sample, the 10 oscillators are placed corresponding to the dots in the XY plane and the FRFs are measured at the six point shown before.

at the nodes of the model. The bottom surface of the plate is marked with the node numbers so that the oscillators can be hung at the nodal locations. The grid numbering scheme is shown Figure 2. This scheme also reduces the uncertainly arising from the measurement of the locations of the oscillators. discrete random number generator is used to generate the X and Y coordinates for the attachment of the oscillators. In total 10 oscillators are used to simulate random unmodelled dynamics. The details of a typical oscillator is shown in Figure 3. The springs are adhesively bonded to a magnet at the top and a mass at the bottom. The magnet at the top of the assembly allows the oscillators to be easily attached to the bottom of the plate. It should be noted that the mass of the magnets would have the 'fixed mass effect' considered in the previous case study on the beam. However, since the plate is much heavier ($\approx$12.5 kg) than the magnets , the effect of the fixed masses (20g in total) is negligible. The stiffness values of the 10 springs used in the experiments are given in Table 2. This table also shows the natural frequency of the individual oscillators. The oscillating mass of each of the 10 oscillators is 121.4g, and hence the total oscillator mass is 1.214 kg, which is 9.8% of the mass of the plate. The springs are attached to the plate at the pre-generated nodal locations using the small magnets located at the top the oscillator assembly. The small magnets (weighting 2g) are found to be strong enough to hold the 121.4g mass attached to the spring below over the frequency range considered. A sample realization of the attached oscillators is shown in Figure 4. ne hundred such realizations of the oscillators are created by hanging the oscillators at random locations and individually tested in this experiment. The variation of the locations of the 10 oscillators are shown in Figure 5.

3   Experimental Methodology

The 32 channel LMS$^{\text{TM}}$ system used in the beam experiment is again employed to perform modal analysis [24–26]. A shaker was used to provide the impulse excitation for the same reasons as the beam experiment (the make, model no., serial no. and sensitivity are given in the previous section). The shaker generated impulses at a pulse increment of 20s and a pulse width of 0.01s. Figure 6 shows the arrangement of the shaker. The shaker is placed so that it impacts at the (4,6) node of the plate. The shaker is driven by a signal from a Simulink$^{\text{TM}}$ and dSpace$^{\text{TM}}$ system via a power amplifier (TPO 25 AEI 00051).

In this experiment six accelerometers are used as the response sensors. The locations of the six sensors are selected such that they cover a broad area of the plate. The locations of the accelerometers are shown in Figure 7. The details of the accelerometers, including their nodal locations, are shown in Table 3. Small holes are drilled into the plate and all of the six accelerometers are attached by bolts through the holes.

Fig. 6. The shaker used to provide an impulse excitation using a Simulink$^{\text{TM}}$and dSpace$^{\text{TM}}$. A hard steel tip was used and the shaker was placed at node (4,6).
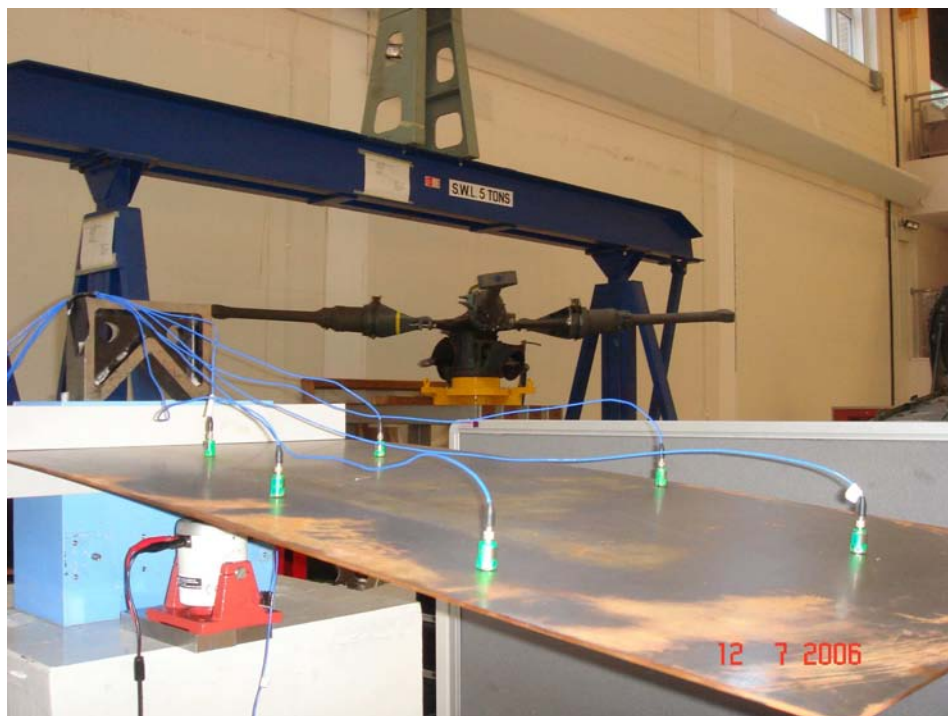
Fig. 7. The positions of the accelerometers on the plate.

Model & Serial number	Coordinates	LMS Channel	Sensitivity
333M07 SN 25948	Point 1: (4,6)	1	98.8 mV/g
333M07 SN 26254	Point 2: (6,11)	2	96.7 mV/g
333M07 SN 26018	Point 3: (11,3)	3	101.2 mV/g
333M07 SN 25942	Point 4: (14,14)	4	97.6 mV/g
333M07 SN 26280	Point 5: (18,2)	5	101.3 mV/g
333M07 SN 26016	Point 6: (21,10)	6	100.0 mV/g

Table 3
The details of the six accelerometers attached to the top of the plate.

The signal from the force transducer is amplified using a KISTLER type 5134 amplifier (with settings Gain: 100, Filter: 10K and Bias: Off) while the signals from the accelerometers are directly input into the LMS system. For data acquisition and processing, LMS Test Lab 5.0 is used. In the Impact Scope, the bandwidth was set to 8192 Hz with 8192 spectral lines (i.e., 1.00 Hz resolution). Five averages are taken for each FRF measurement. The steel tip used in the experiment only gives clean data up to approximately 4500 Hz. As a result 4000 Hz was used as the upper limit of the frequency in the measured frequency response functions. The data logged beyond 4000 Hz should be ignored for this experiment.

4   Results and Discussions

4.1   Amplitude spectra

In this paper we will discuss results corresponding to point 1 (the driving-point FRF) and point 2 (a cross FRF) only. Results for the other points are not shown to save space but can be obtained from the uploaded data file. Figure 8 shows the amplitude of the frequency response function (FRF) at point 1 (see Table 3 for the location) of the plate without any oscillators (the baseline model). In the same figure 100 samples of the amplitude of the FRF are shown together with the ensemble mean, 5% and 95% probability lines. In figures 8(b)-(d) we have separately shown the low, medium and high-frequency response, obtained by zooming around the appropriate frequency ranges in Figure 8(a). There are of course no fixed and definite boundaries between the low, medium and high-frequency ranges. Here we have selected $0 - 1.0$kHz as the low-frequency vibration, $1.0 - 2.5$kHz as the medium-frequency vibration and $2.5 - 4$kHz as the high-frequency vibration. These frequency boundaries are selected on the basis of the qualitative nature of the response and devised purely for the presentation of the results. The experimental approach discussed here is independent on these selections. The measured FRF data up to 4.0 KHz as shown here is significantly noise-free,
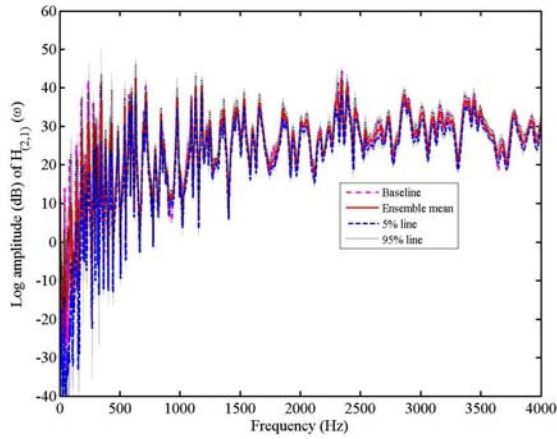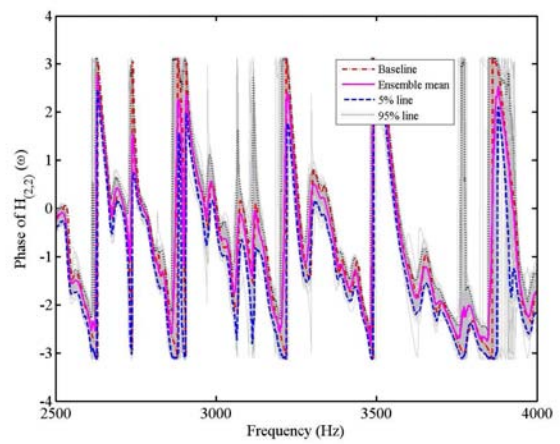
(a) Response across the frequency range
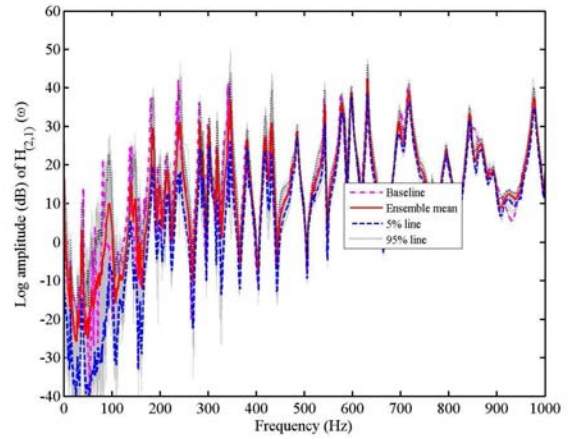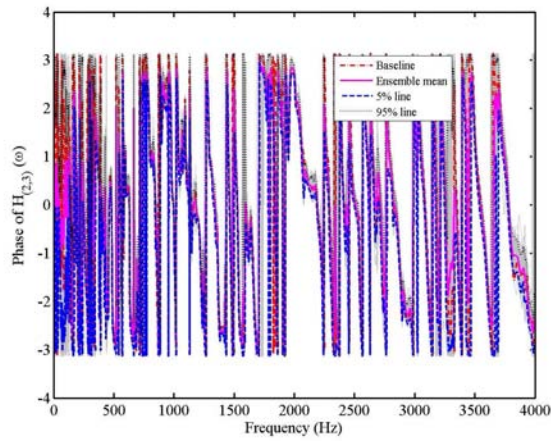
(b) Low-frequency response
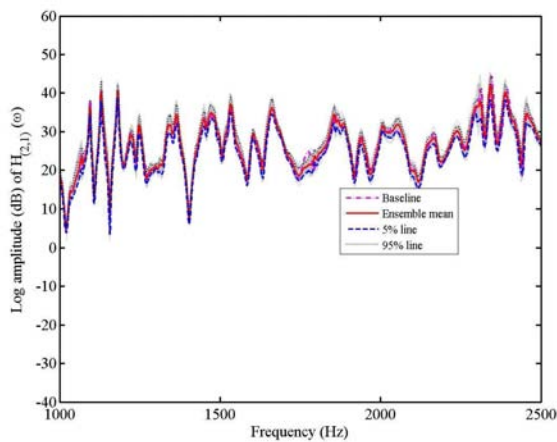
(c) Medium-frequency response
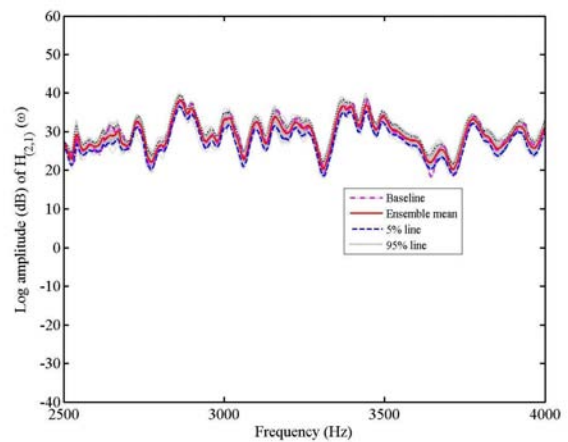
(d) High-frequency response

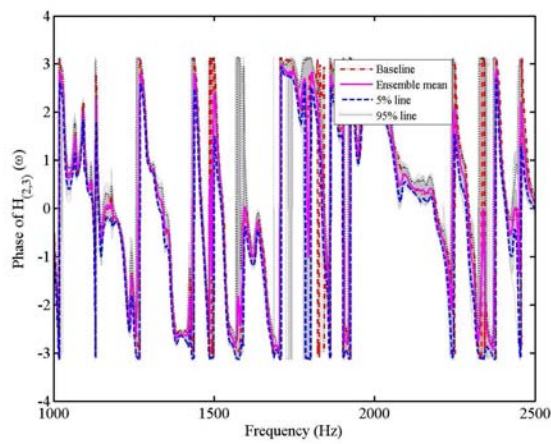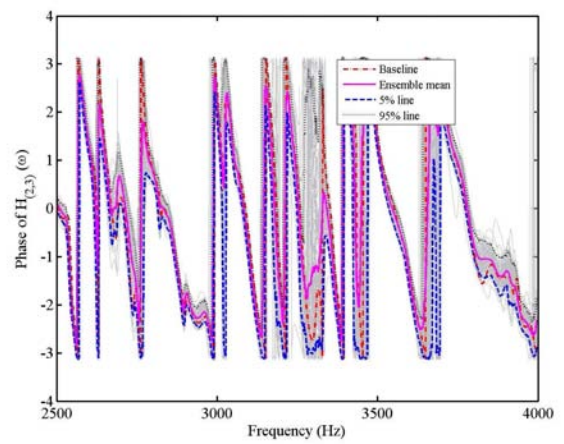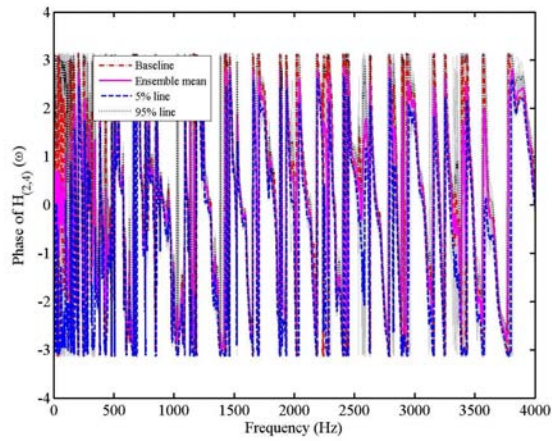Fig. 8. Experimentally measured amplitude of the driving-point FRF of the plate at point 1 (nodal coordinate: (4,6)) with 10 randomly placed oscillators. 100 FRFs, together with the ensemble mean, 5% and 95% probability points are shown.

since the hard steel tip used was able to excite the whole frequency range. The experimental data shown throughout the paper is the 'raw data' (that is, without any filtering) obtained directly from the LMS system. The ensemble mean follows the result of the baseline system closely except in the low frequency range. The relative variance of the amplitude of the FRF remains more or less constant in the mid and high frequency range. Equivalent results for the cross FRF at point 2 (see Table 3 for the locations) are shown in Figure 9. The general trend of the results is similar to that of point 1 except that the response variability is slightly more. Note that most of the variability in the FRFs is concentrated at the low frequency region. This is because the frequency of the attached oscillators at random locations are below 70 Hz.
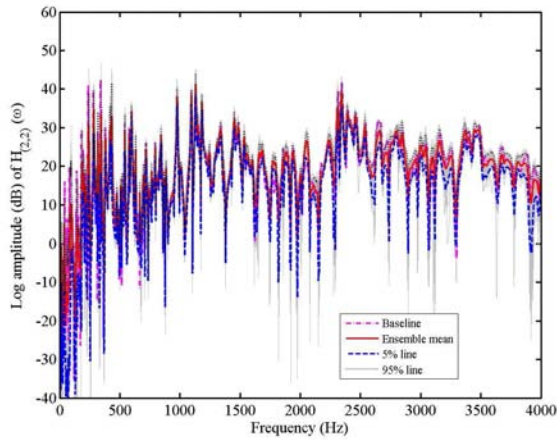
(a) Response across the frequency range
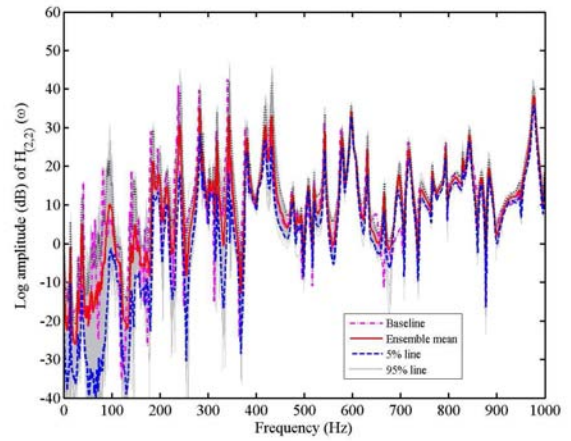
(b) Low-frequency response
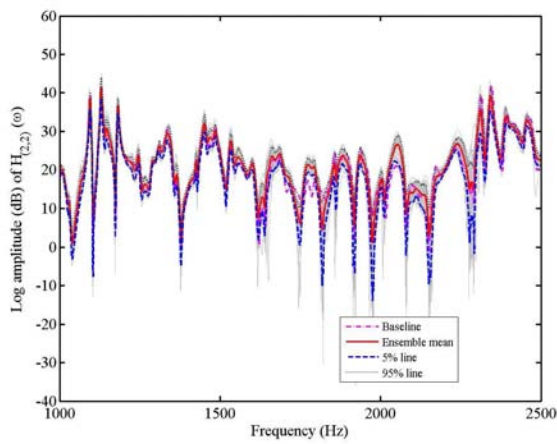
(c) Medium-frequency response
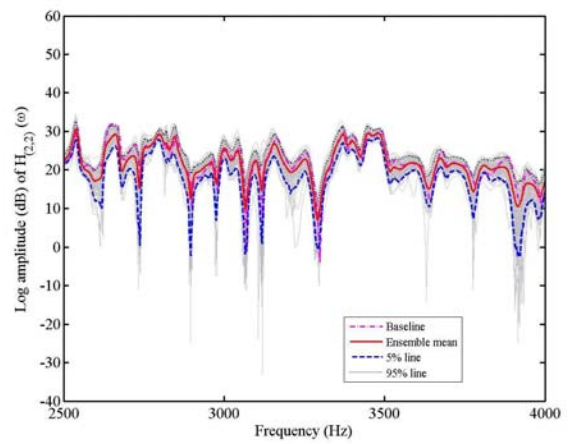
(d) High-frequency response

Fig. 9. Experimentally measured amplitude of the cross-FRF of the plate at point 2 (nodal coordinate: (6,11)) with 10 randomly placed oscillators. 100 FRFs, together with the ensemble mean, 5% and 95% probability points are shown.
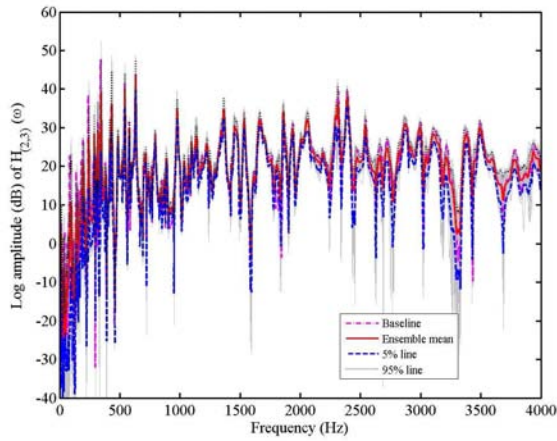
(a) Response across the frequency range
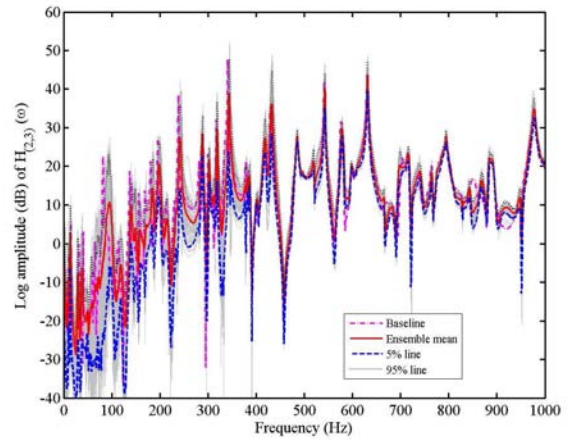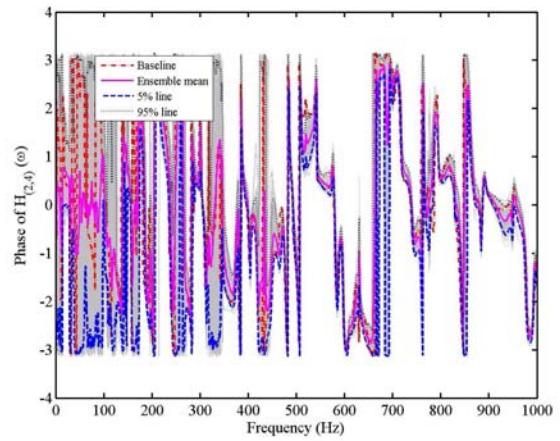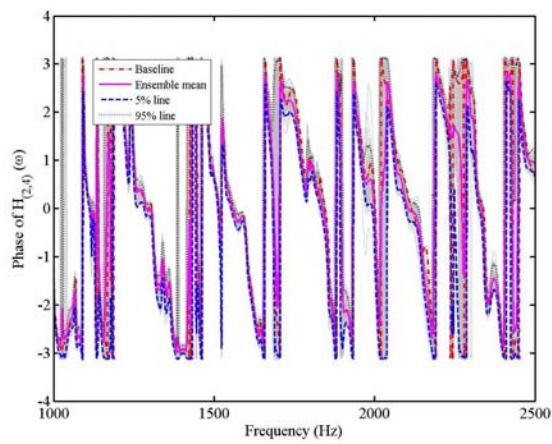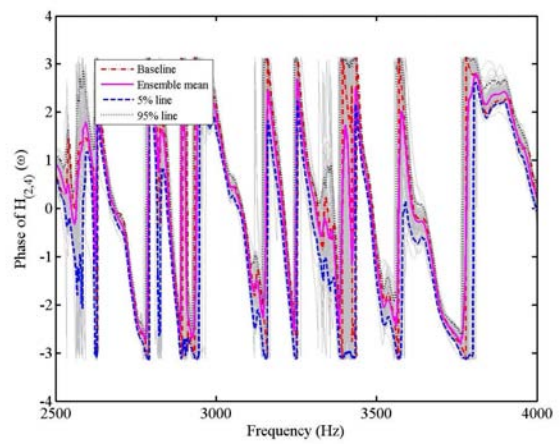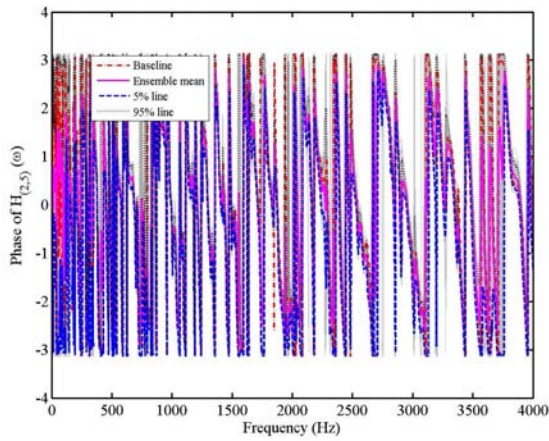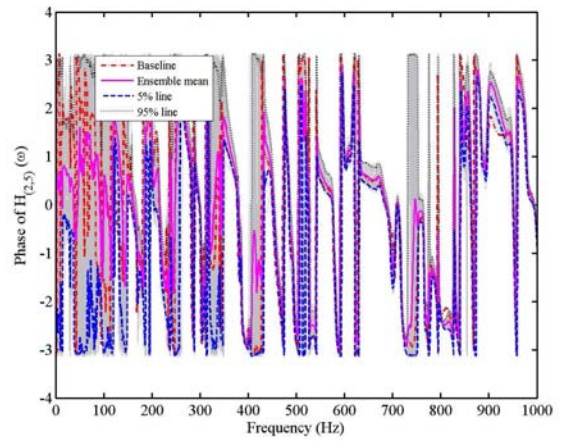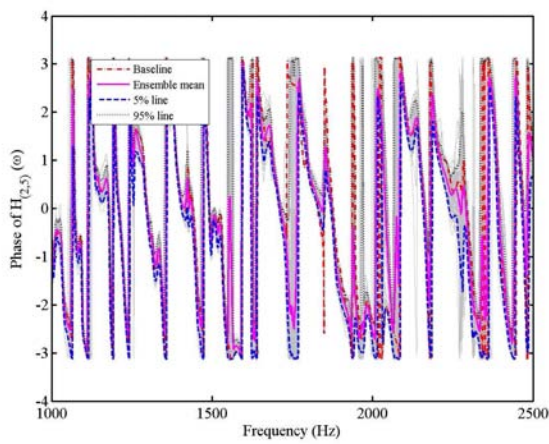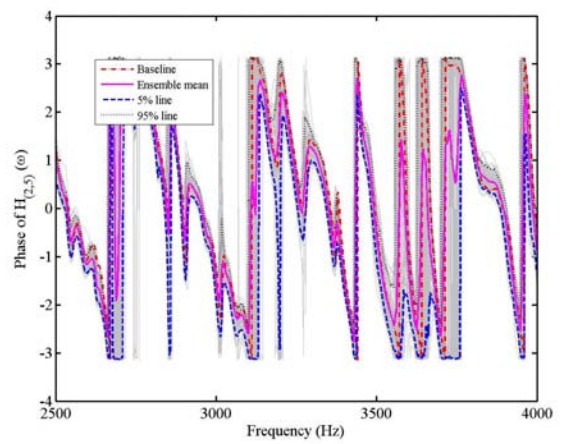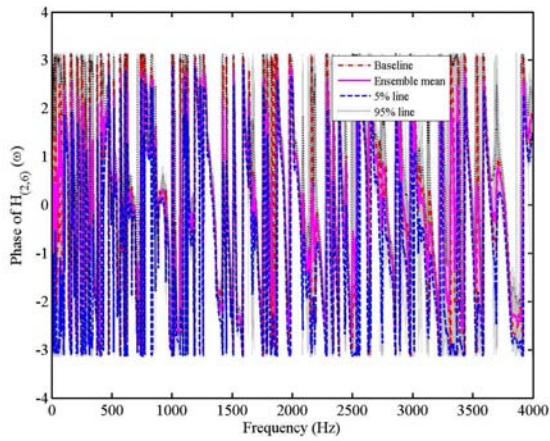
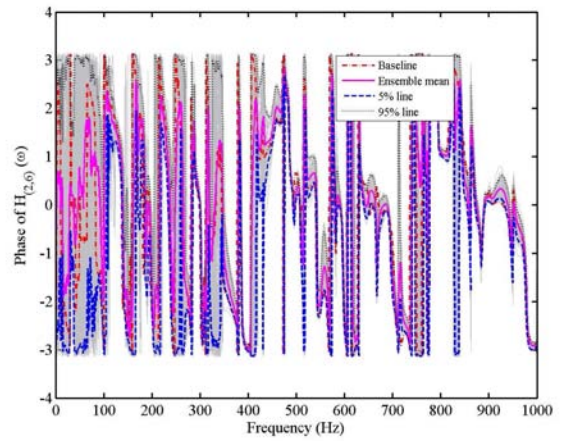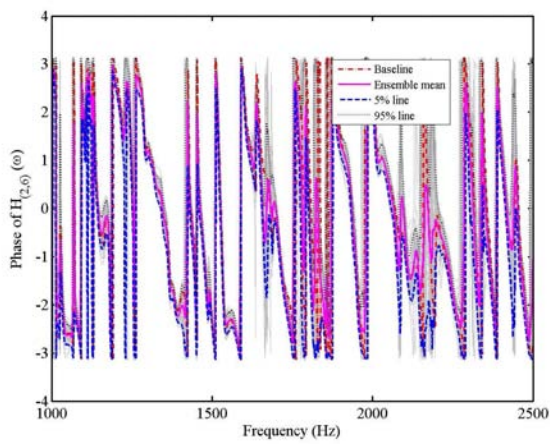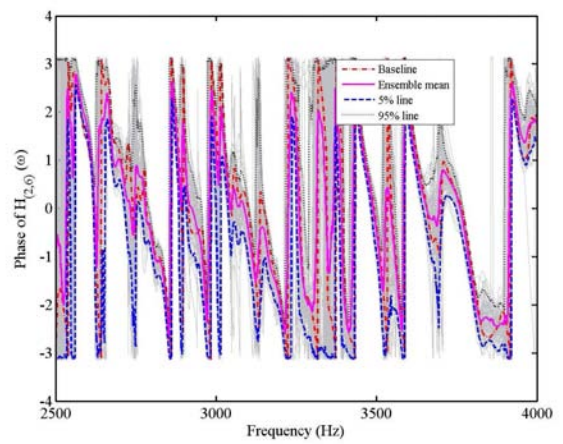(b) Low-frequency response
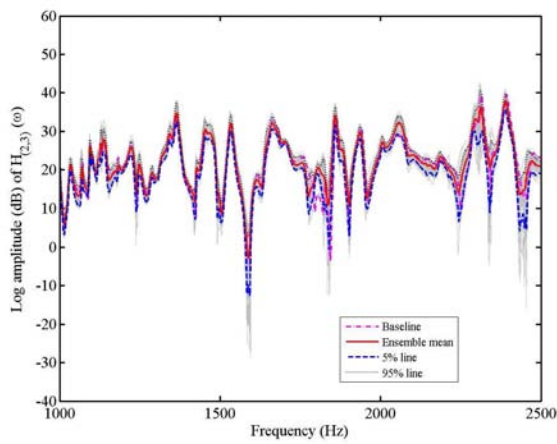
(c) Medium-frequency response
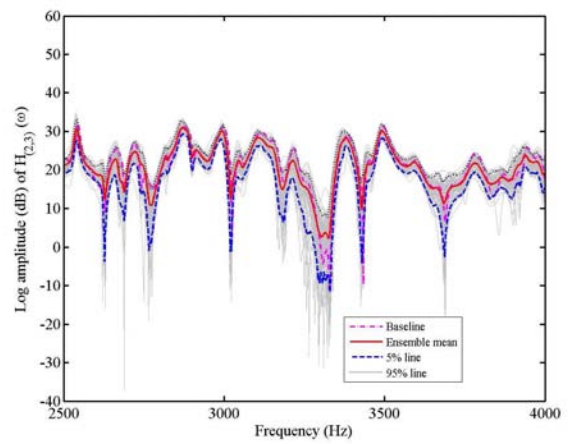
(d) High-frequency response

Fig. 10. Experimentally measured amplitude of the cross-FRF of the plate at point 3 (nodal coordinate: (11,3)) with 10 randomly placed oscillators. 100 FRFs, together with the ensemble mean, 5% and 95% probability points are shown.
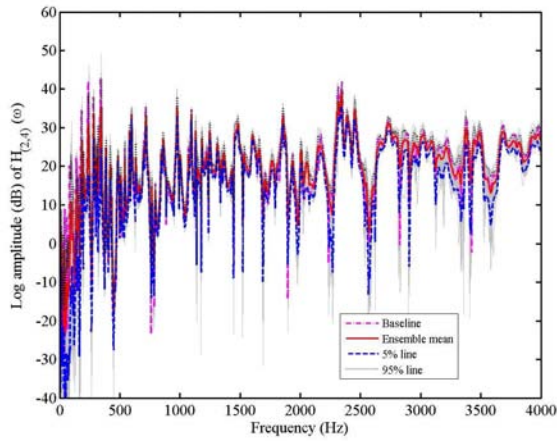
(a) Response across the frequency range
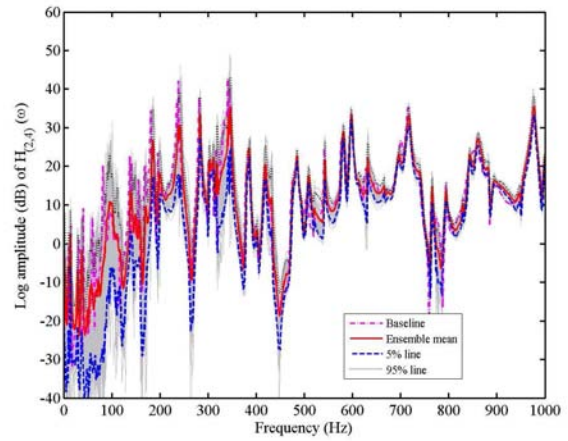
(b) Low-frequency response
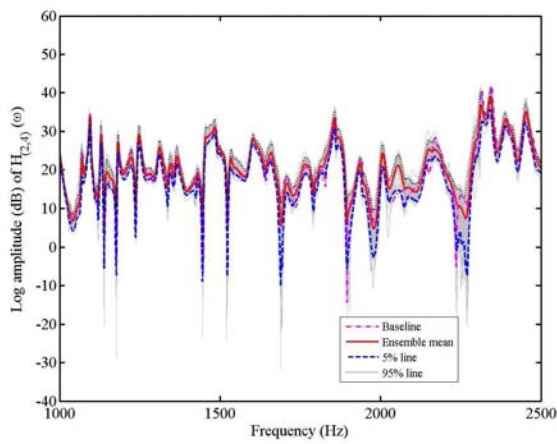
(c) Medium-frequency response
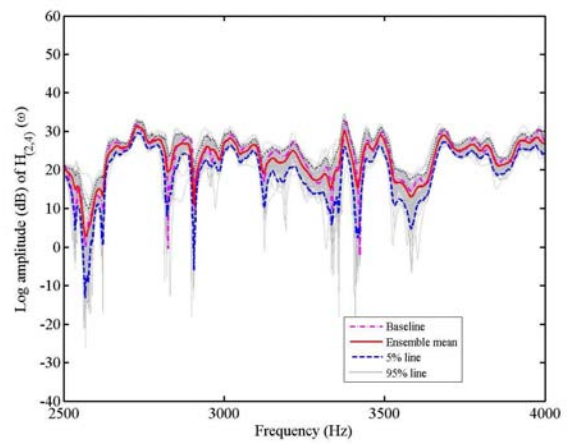
(d) High-frequency response

Fig. 11. Experimentally measured amplitude of the cross-FRF of the plate at point 4 (nodal coordinate: (14,14)) with 10 randomly placed oscillators. 100 FRFs, together with the ensemble mean, 5% and 95% probability points are shown.
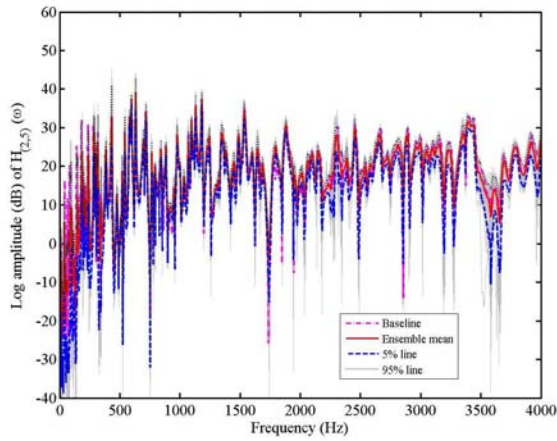
(a) Response across the frequency range
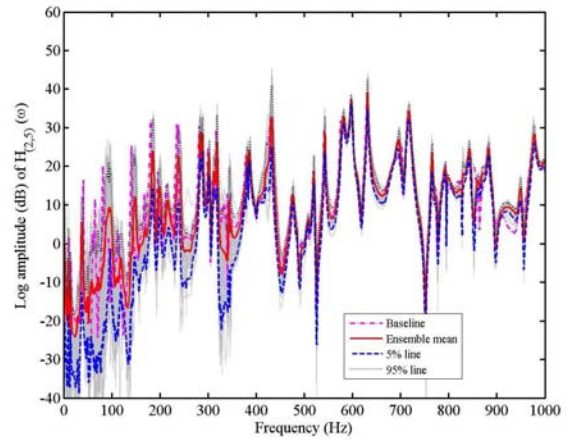
(b) Low-frequency response
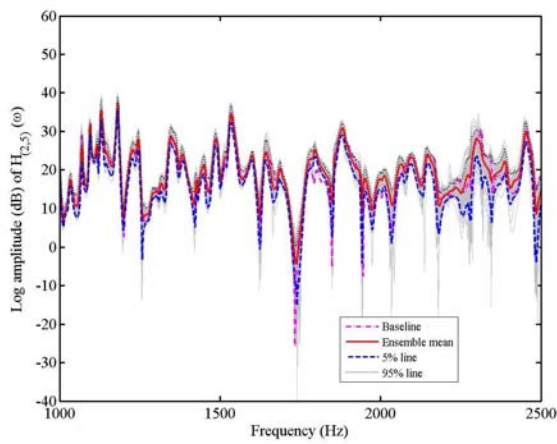
(c) Medium-frequency response
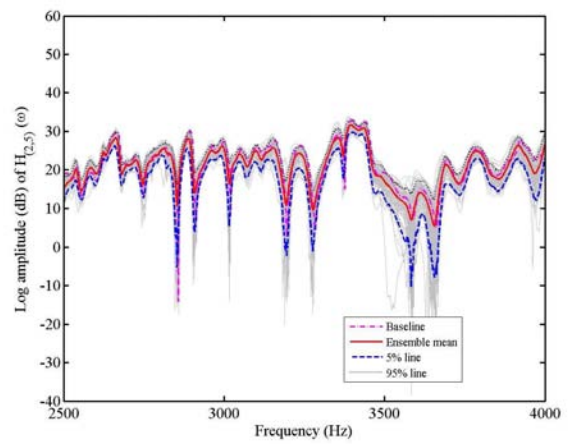
(d) High-frequency response

Fig. 12. Experimentally measured amplitude of the cross-FRF of the plate at point 5 (nodal coordinate: (18,2)) with 10 randomly placed oscillators. 100 FRFs, together with the ensemble mean, 5% and 95% probability points are shown.
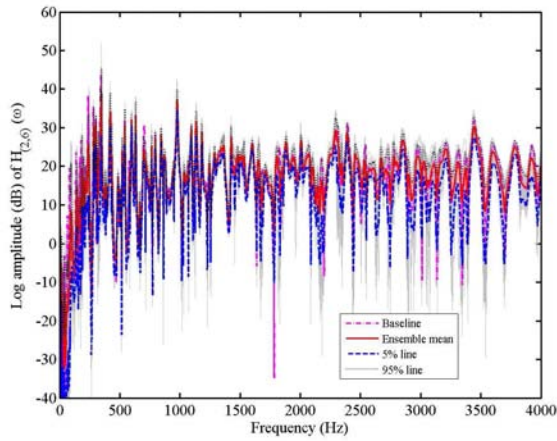
(a) Response across the frequency range
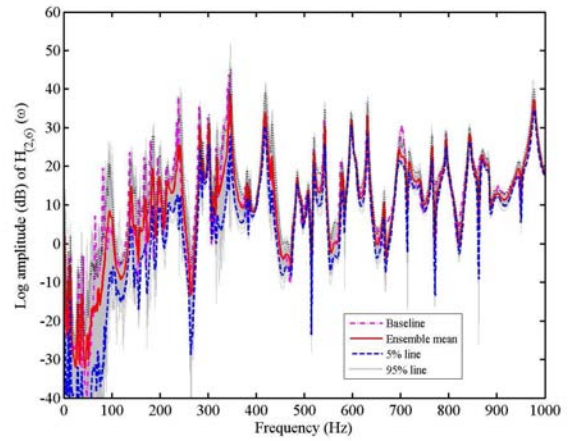
(b) Low-frequency response
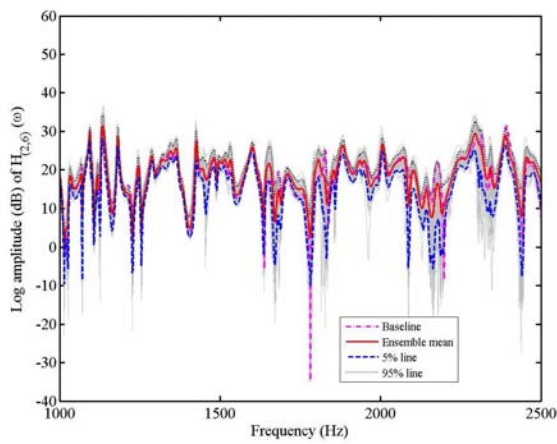
(c) Medium-frequency response
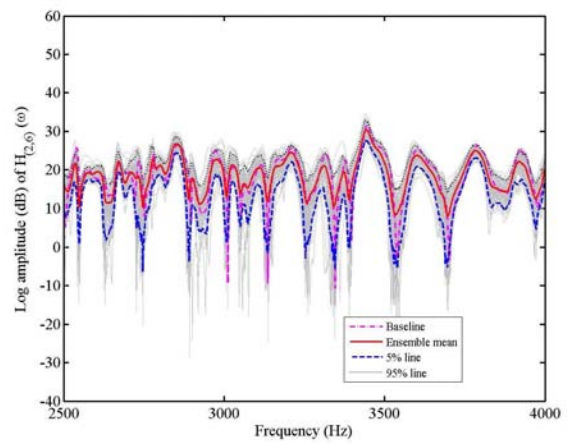
(d) High-frequency response

Fig. 13. Experimentally measured amplitude of the cross-FRF of the plate at point 6 (nodal coordinate: (21,10)) with 10 randomly placed oscillators. 100 FRFs, together with the ensemble mean, 5% and 95% probability points are shown.
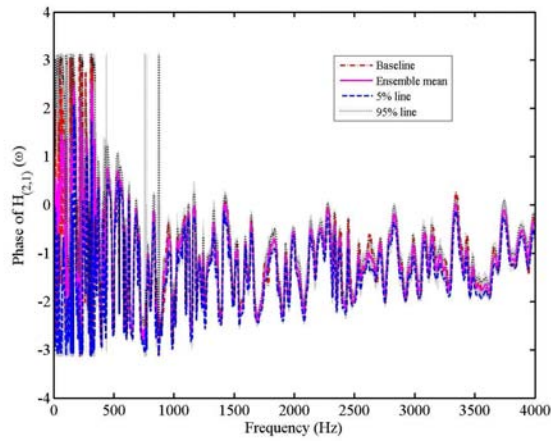
(a) Phase across the frequency range
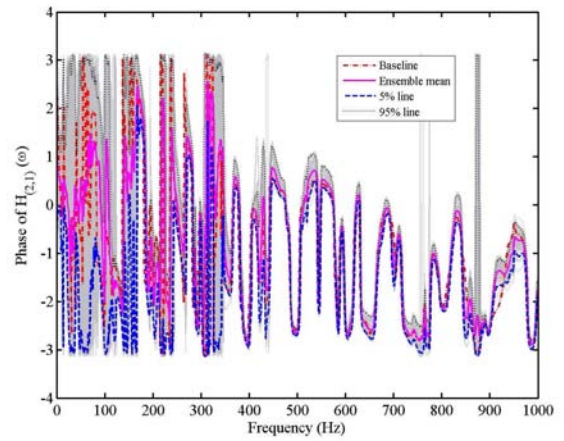
(b) Low-frequency response
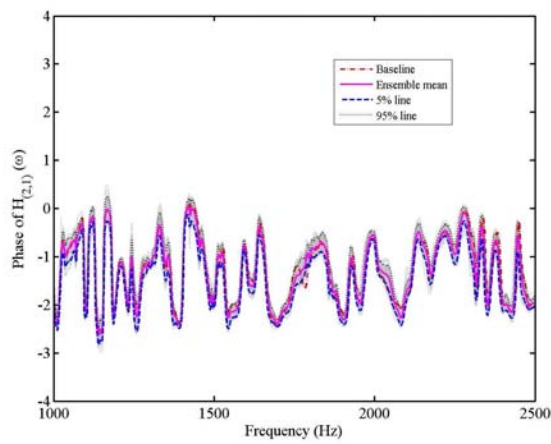
(c) Medium-frequency response
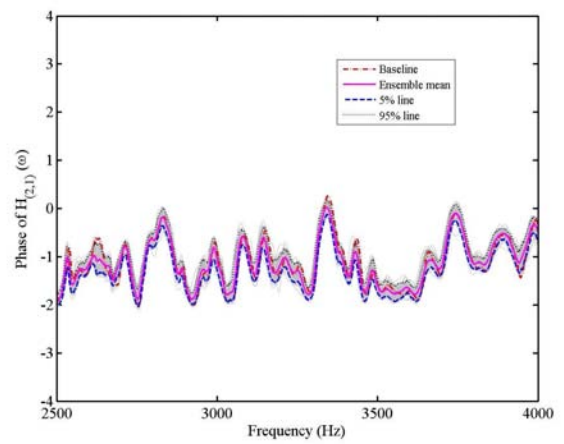
(d) High-frequency response

Fig. 14. Experimentally measured phase of the driving-point FRF of the plate at point 1 (nodal coordinate: (4,6)) with 10 randomly placed oscillators. 100 FRFs, together with the ensemble mean, 5% and 95% probability points are shown.

Figure 14 shows the phase of the frequency response function (FRF) at point 1 (the driving-point FRF, see Table 3 for the location) of the plate without any oscillators (the baseline model). In the same figure 100 samples of the phase of the FRF are shown together with the ensemble mean, 5% and 95% probability lines. igures 14(b)-(d) show the phase in low, medium and high-frequency separately, obtained by zooming around the appropriate frequency ranges in Figure 14(a). The ensemble mean follows the result of the baseline system closely except in the low frequency range. This is again due to the fact that the frequency of the attached oscillators at random locations are below 70 Hz.

The relative variability of the phase of the FRF remains more or less constant in the mid and high frequency ranges. Equivalent results for point 2 (a cross-FRF, see Table 3 for the location) are shown in Figure 15. Because this is the phase of a cross-FRF, its general characteristics is different from the driving-point FRF shown in Figure 14. The variability is also observed to be slightly higher compared to the phase of the driving-point FRF.

5 Numerical Simulation

In this section we aim to numerically simulate the experimental system discussed in section 2. The objective here is to see whether the pattern of uncertainty in the response observed in the experiment can be observed using the standard Monte Carlo simulation approach often used in probabilistic mechanics. A steel cantilever plate with homogeneous geometric (i.e. uniform thickness) and constitutive properties (i.e. uniform Young's modulus and Poisson's ratio) is considered. The numerical values of the material properties are given in Table 1. This uniform plate simulates the *baseline* system shown in Figure 1. The diagram of the plate together with the numerical values assumed for the system parameters are shown in Figure 20. The plate is excited by an unit harmonic force and the responses are calculated at the points shown in the diagram. he input node corresponds to the location of the shake shown in Figure 6 and the output nodes correspond to the locations of the accelerometers shown in Figure 7. The baseline model is perturbed by a set of sprung-mass oscillators, each having natural frequency according to Table 2 and attached randomly along the plate. The one hundred sets of coordinates of the ten oscillators employed in the experiment (as shown in Figure 5) is again used here.

In the numerical calculations 375 elements are used and the resulting finite element model has 1200 degrees-of-freedom. Only first 720 modes are used in the calculation of the frequency response functions. Figure 21 shows the mean and standard deviation of the natural frequencies of the beam obtained using Monte Carlo simulation. rom Figure 21 observe that the
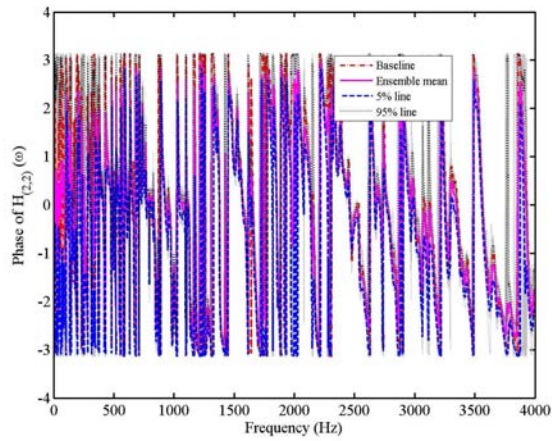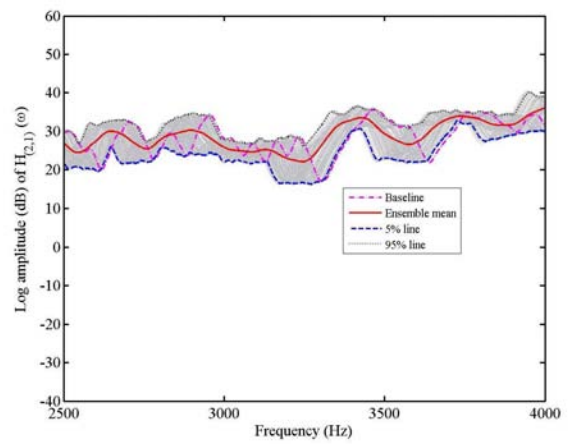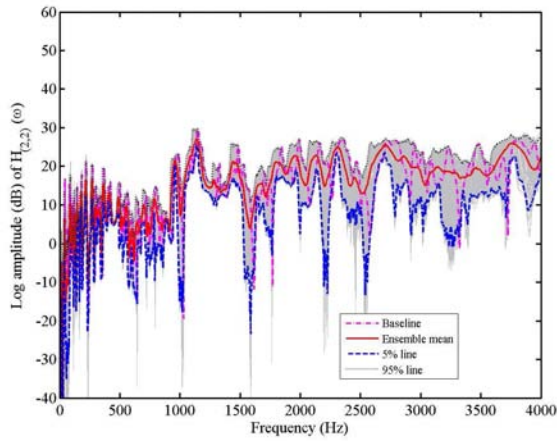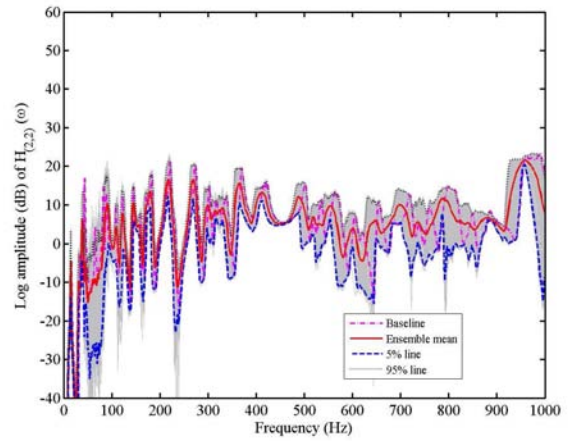
(a) Response across the frequency range
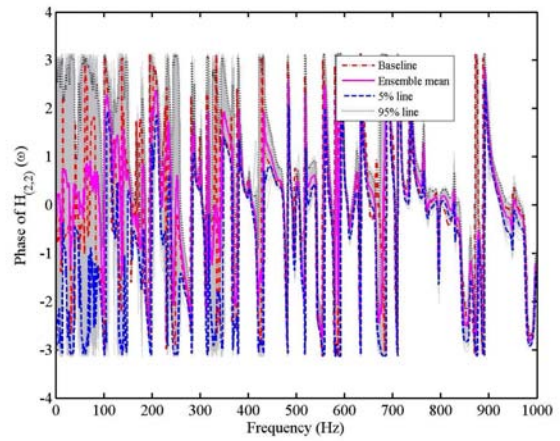
(b) Low-frequency response
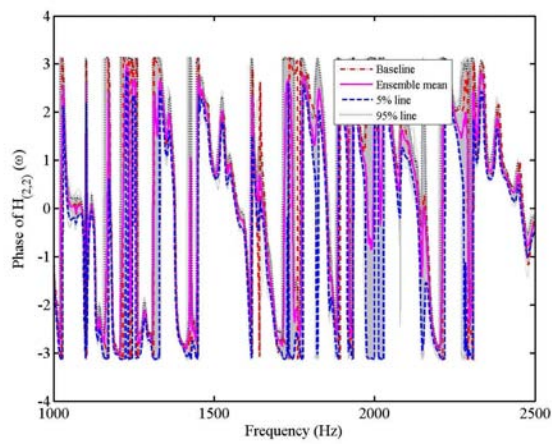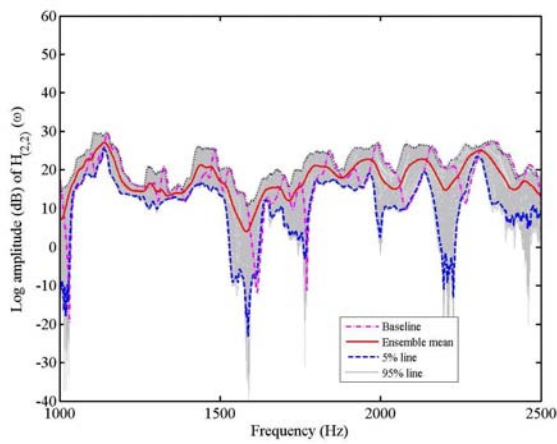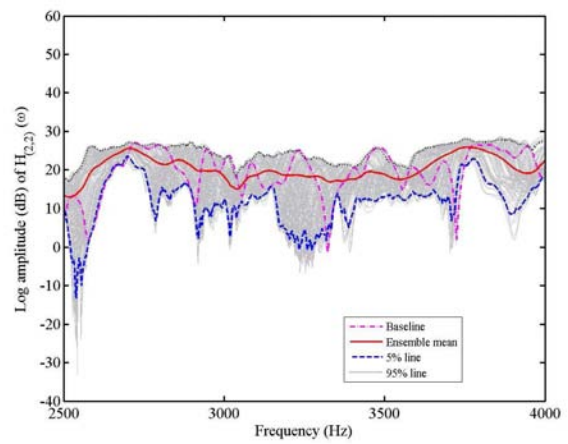
(c) Medium-frequency response

(d) High-frequency response

Fig. 15. Experimentally measured phase of the cross-FRF of the plate at point 2 (nodal coordinate: (6,11)) with 10 randomly placed oscillators. 100 FRFs, together with the ensemble mean, 5% and 95% probability points are shown.

(a) Response across the frequency range
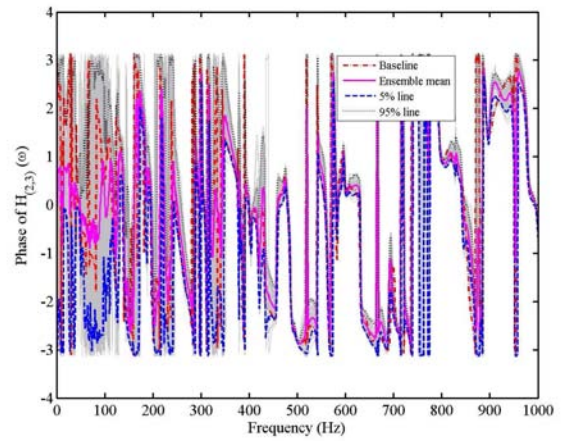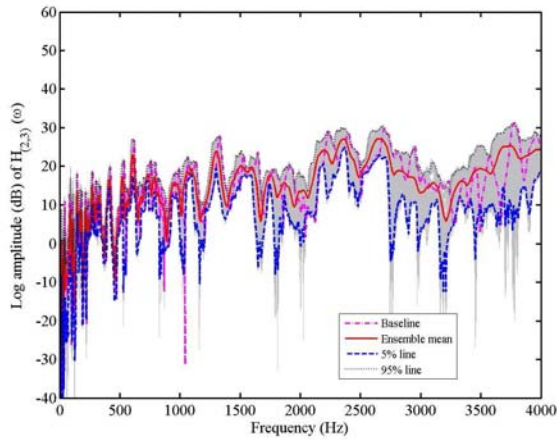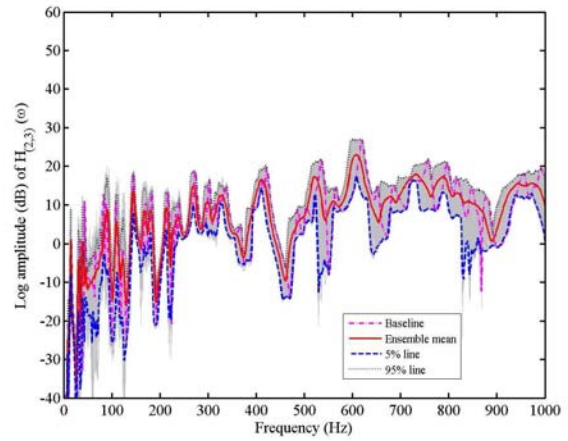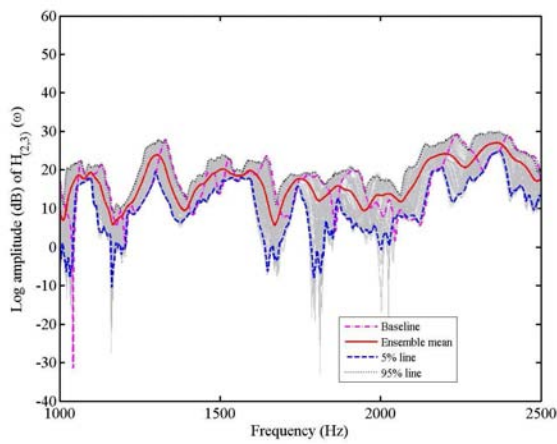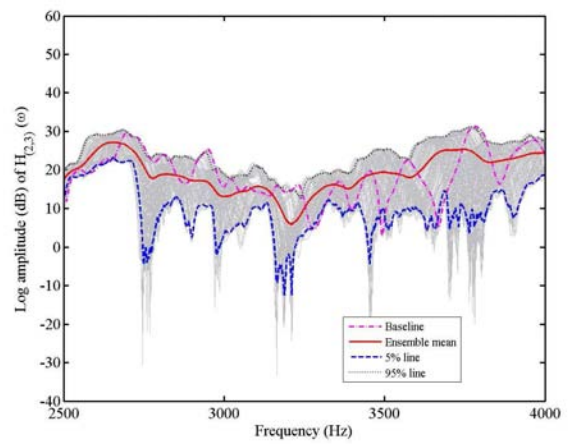
(b) Low-frequency response

(c) Medium-frequency response

(d) High-frequency response

Fig. 16. Experimentally measured phase of the cross-FRF of the plate at point 3 (nodal coordinate: (11,3)) with 10 randomly placed oscillators. 100 FRFs, together with the ensemble mean, 5% and 95% probability points are shown.

(a) Response across the frequency range
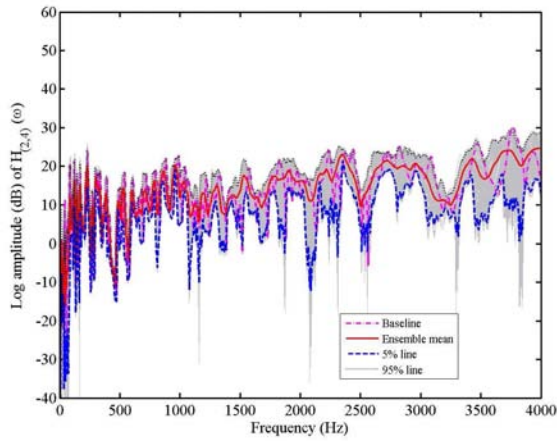
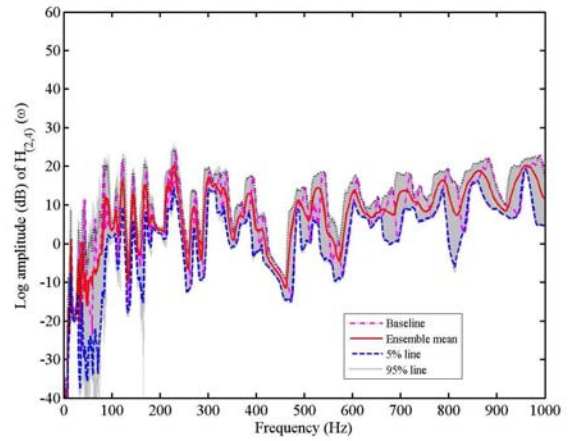(b) Low-frequency response

(c) Medium-frequency response

(d) High-frequency response

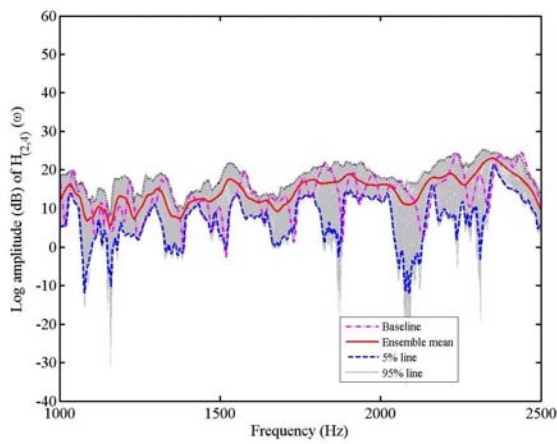Fig. 17. Experimentally measured phase of the cross-FRF of the plate at point 4 (nodal coordinate: (14,14)) with 10 randomly placed oscillators. 100 FRFs, together with the ensemble mean, 5% and 95% probability points are shown.
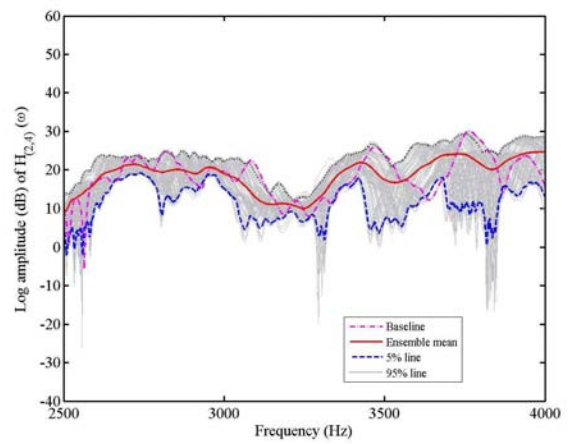
(a) Response across the frequency range
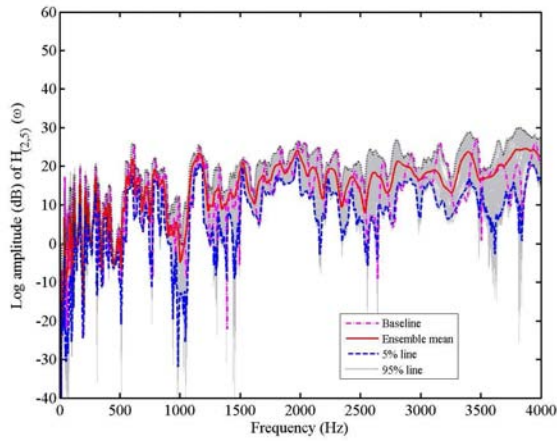
(b) Low-frequency response

(c) Medium-frequency response

(d) High-frequency response

Fig. 18. Experimentally measured phase of the cross-FRF of the plate at point 5 (nodal coordinate: (18,2)) with 10 randomly placed oscillators. 100 FRFs, together with the ensemble mean, 5% and 95% probability points are shown.

(a) Response across the frequency range

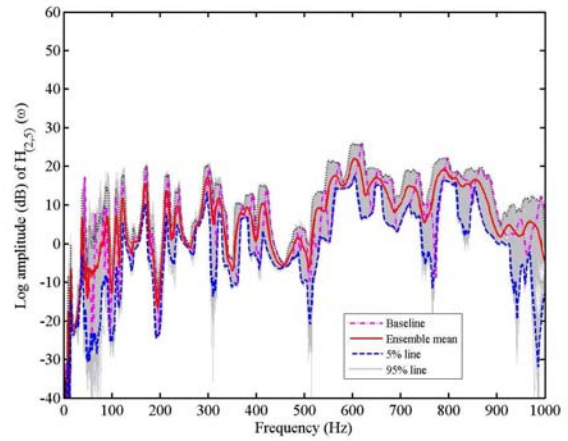(b) Low-frequency response

(c) Medium-frequency response

(d) High-frequency response

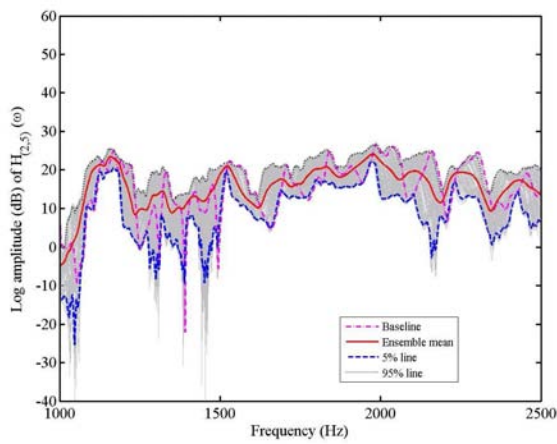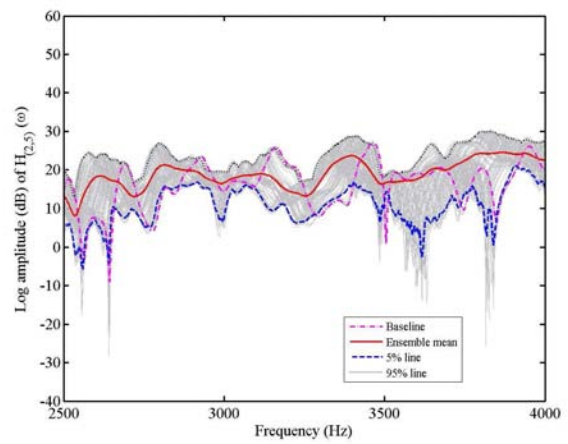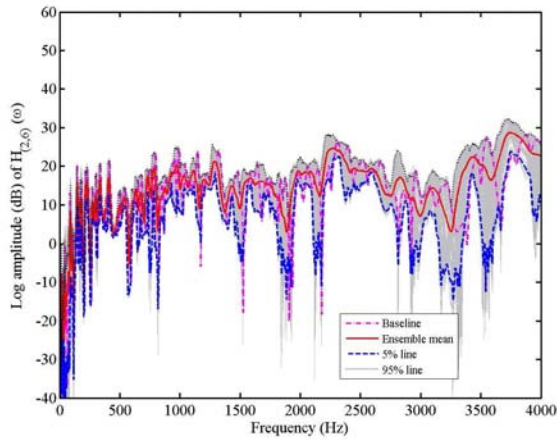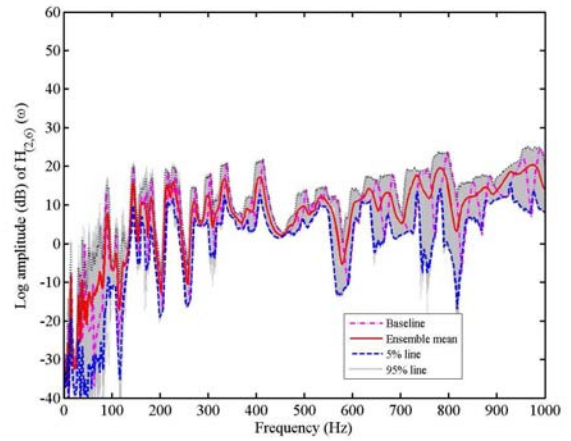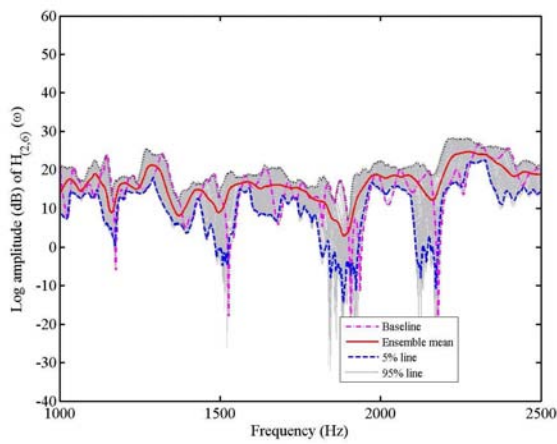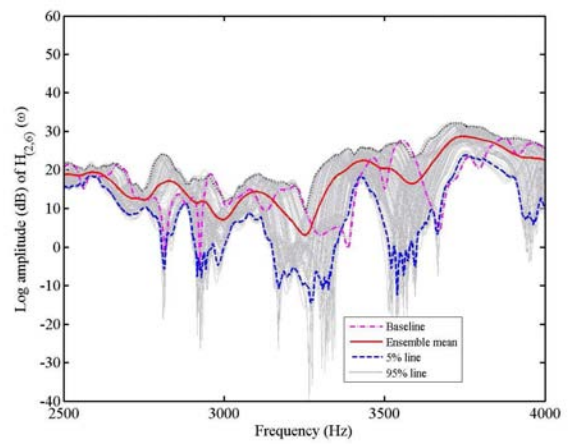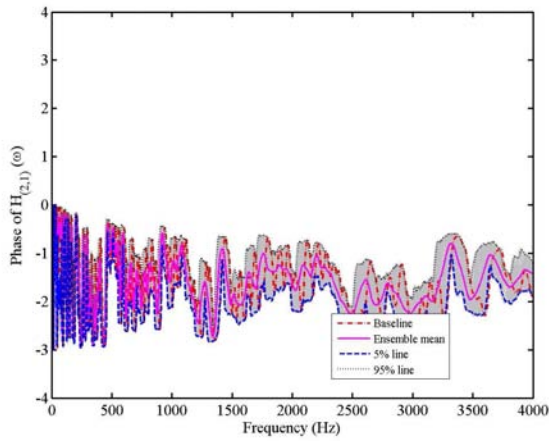Fig. 19. Experimentally measured phase of the cross-FRF of the plate at point 6 (nodal coordinate: (21,10)) with 10 randomly placed oscillators. 100 FRFs, together with the ensemble mean, 5% and 95% probability points are shown.
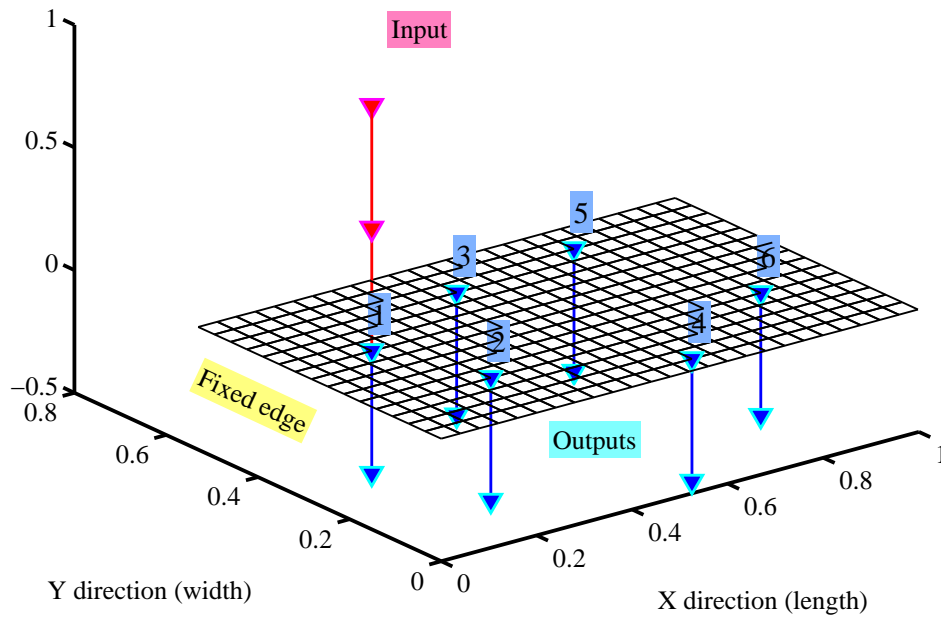
Fig. 20. The Finite Element (FE) model of a steel cantilever plate: 25×15 elements, 416 nodes, 1200 degrees-of-freedom. The material and geometric properties are: $E = 200 \times 10^9 \mathrm{N/m^2}$, $\mu = 0.3$, $\rho = 7860$ kg/m^3, $t_h = 3.0$mm, $L_x = 0.998$m, $L_y = 0.53$m. Input node number: 481, Output node numbers: 481, 877, 268, 1135, 211 and 844, 0.7% modal damping is assumed for all modes.
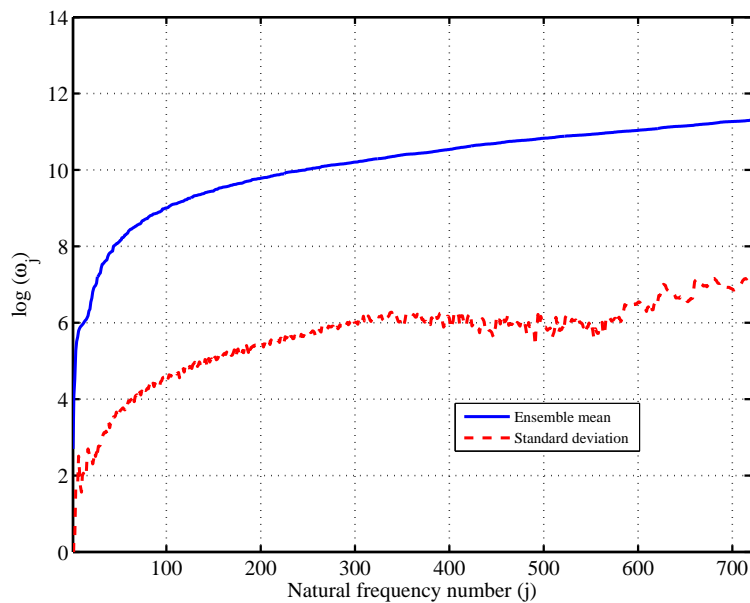
Fig. 21. Mean and standard deviation of the natural frequencies of the plate with randomly placed oscillators.
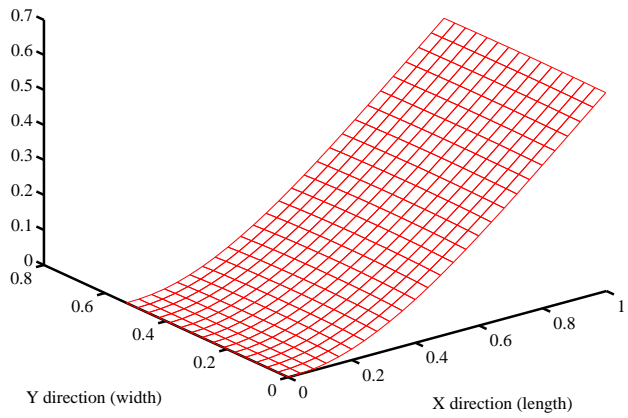
(a) $\omega_{0_1} = 2.5190\text{Hz}$, $\bar{\omega}_1 = 2.3593\text{Hz}$, $\sigma_1 = 0.0482\text{Hz}$
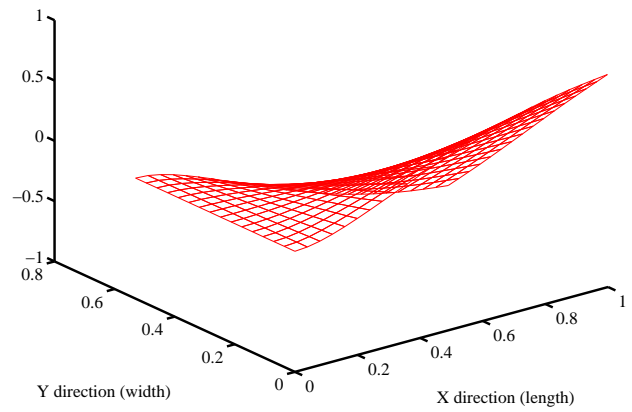
(b) $\omega_{0_2} = 10.2922\text{Hz}$, $\bar{\omega}_2 = 9.5892\text{Hz}$, $\sigma_2 = 0.2334\text{Hz}$
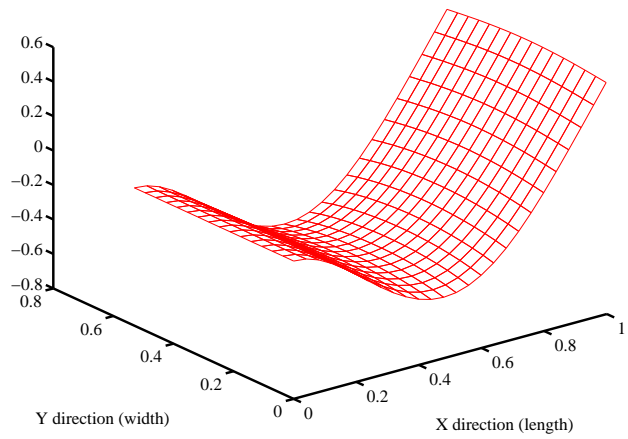
(c) $\omega_{0_3} = 15.6964\text{Hz}$, $\bar{\omega}_3 = 14.6502\text{Hz}$, $\sigma_3 = 0.2321\text{Hz}$
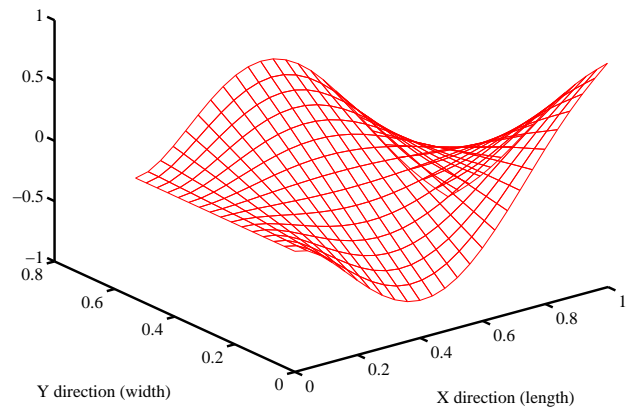
(d) $\omega_{0_4} = 33.7278\text{Hz}$, $\bar{\omega}_4 = 30.9462\text{Hz}$, $\sigma_4 = 0.8830\text{Hz}$
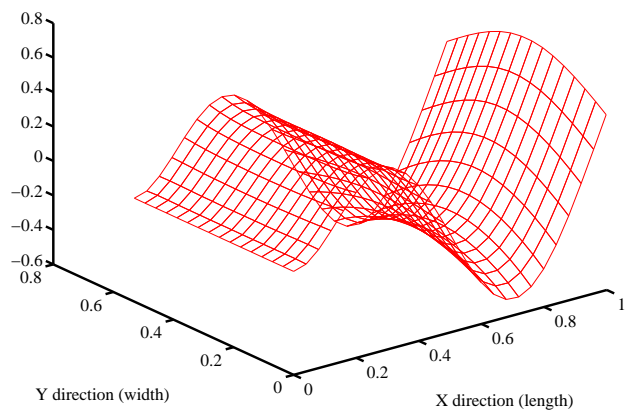
(e) $\omega_{0_5} = 44.0050\text{Hz}$, $\bar{\omega}_5 = 39.4086\text{Hz}$, $\sigma_5 = 00.8869\text{Hz}$
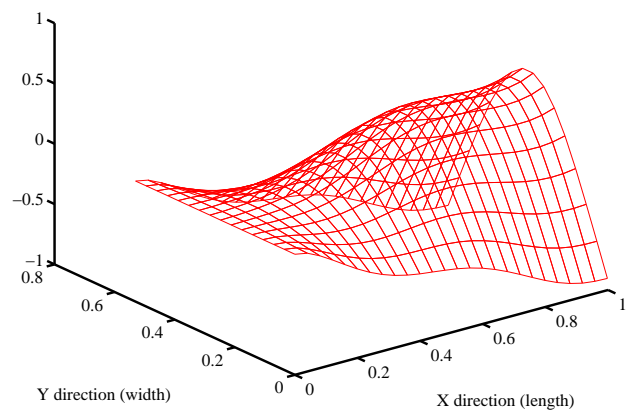
(f) $\omega_{0_6} = 60.9846\text{Hz}$, $\bar{\omega}_6 = 44.3053\text{Hz}$, $\sigma_6 = 0.9390\text{Hz}$

Fig. 22. First six mode shapes and natural frequencies of the baseline model together with the mean and standard deviation of the natural frequencies obtained form 100 realizations of 10 randomly placed oscillators.

standard deviation of the natural frequencies are quite small compared to the mean values. The slight variations of the natural frequencies at the lower frequencies correspond to the natural frequencies of the attached oscillators. Natural frequencies and model shapes of the baseline model together with the mean and standard deviation of the first six natural frequencies are shown in Figure 22. ote that the natural frequencies of the baseline model is lower that the mean natural frequencies of the plate with randomly placed oscillators. This is because if the fact the baseline system has lower mass compared to the plate with oscillators.

5.1 Amplitude spectra

For the frequency response function calculation, a modal damping factor of 0.7% is assumed for all of the modes. Figure 23 shows the amplitude of the frequency response function (FRF) at point 1 (the driving-point FRF, see Table 3 for the location) of the plate without any oscillators (the baseline model). In the same figure 100 samples of the amplitude of the FRF are shown together with the ensemble mean, 5% and 95% probability lines. n figures 23(b)-(d) we have separately shown the low, medium and high-frequency response, obtained by zooming around the appropriate frequency ranges in Figure 23(a). The ensemble mean does not follow the result of the baseline system closely in any frequency range. The relative variance of the amplitude of the FRF remains more or less constant in the mid and high frequency range. Equivalent results for the cross FRF at point 2 (see Table 3 for the locations) are shown in Figure 24. he general statistical trend of the results is similar to that of point 1 except that the response variability is slightly more. Significant variability in the FRFs can be seen at the low frequency region. This is because the frequency of the attached oscillators at random locations are below 70 Hz.

5.2 Phase spectra

Figure 29 shows the phase of the frequency response function (FRF) at point 1 (see Table 3 for the location) of the plate without any oscillators (the baseline model). In the same figure 100 samples of the phase of the FRF are shown together with the ensemble mean, 5% and 95% probability lines. igures 29(b)-(d) show the phase in low, medium and high-frequency separately, obtained by zooming around the appropriate frequency ranges in Figure 29(a). In general the ensemble mean does not follow the result of the baseline system. The relative variability of the phase of the FRF remains more or less constant in the mid and high frequency ranges. Equivalent results for point 2 (a cross-FRF, see Table 3 for the location) are shown in Figure 15. Because this is the phase of a cross-FRF, its general characteristics is different from the driving-point FRF shown in Figure 14. The variability is also observed to be slightly
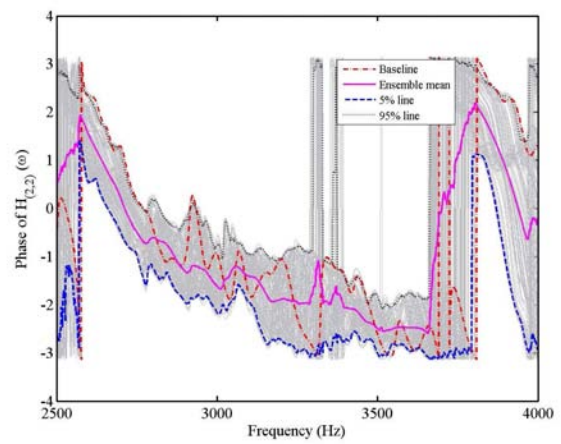
(a) Response across the frequency range
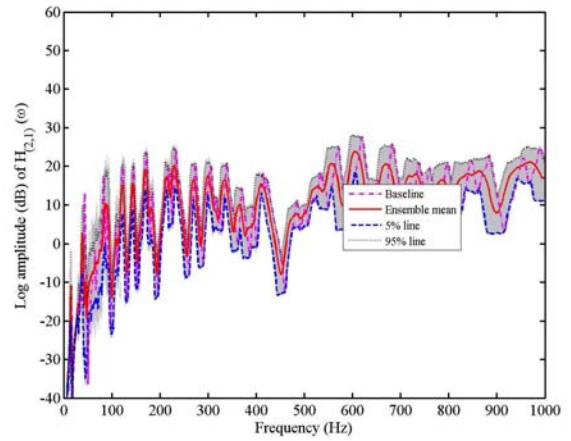
(b) Low-frequency response
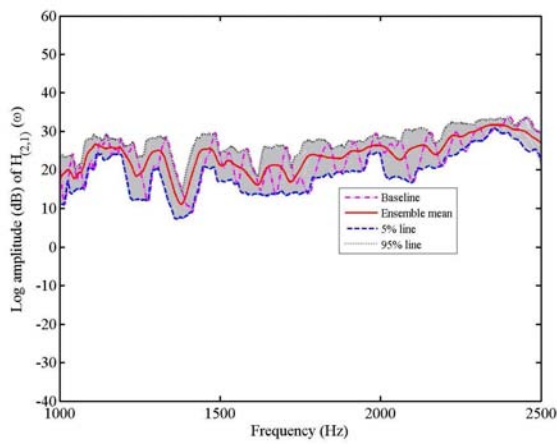
(c) Medium-frequency response

(d) High-frequency response

Fig. 23. Numerically calculated amplitude of the driving-point FRF of the plate at point 1 (nodal coordinate: (4,6)) with 10 randomly placed oscillators. 100 FRFs, together with the ensemble mean, 5% and 95% probability points are shown.

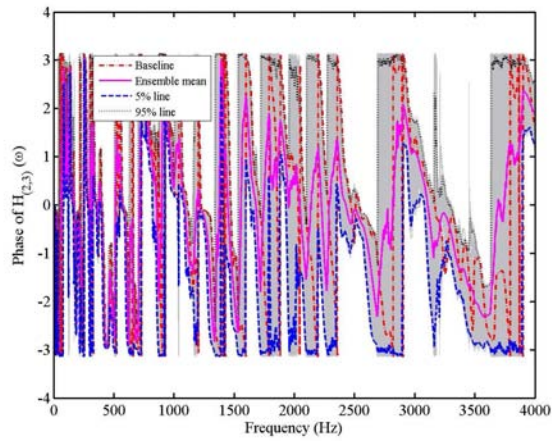(a) Response across the frequency range
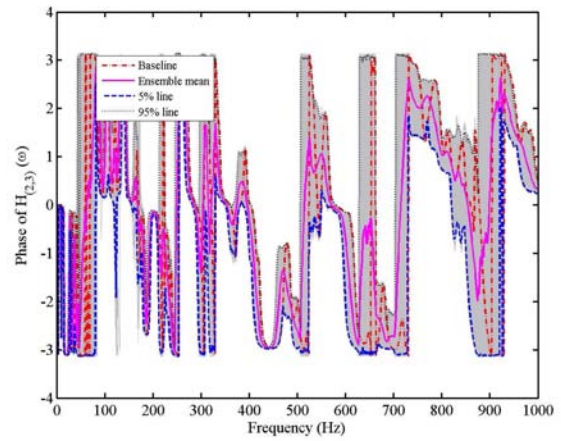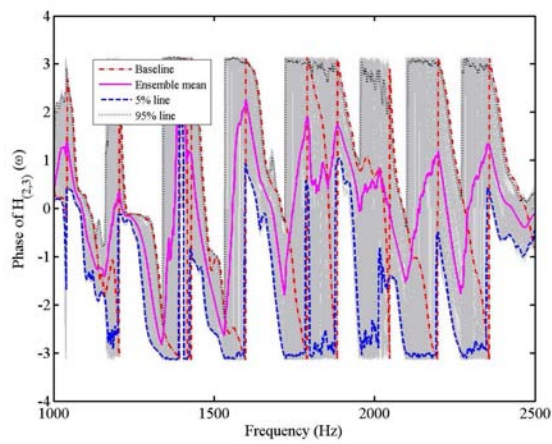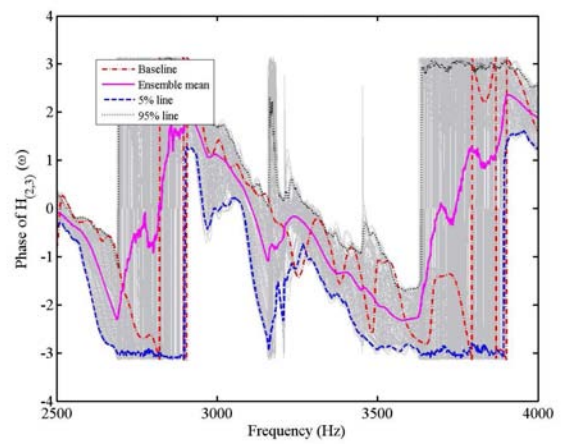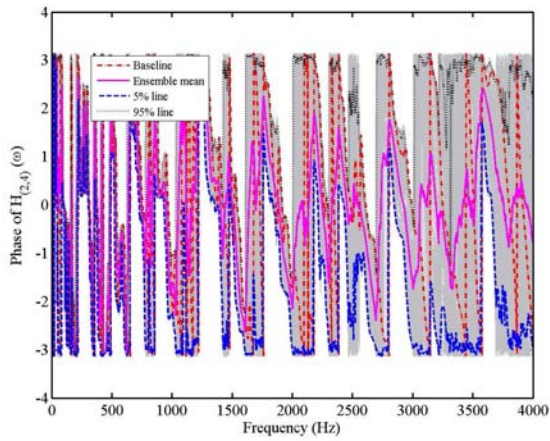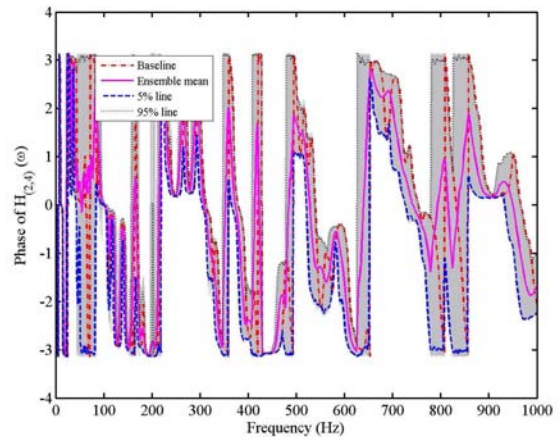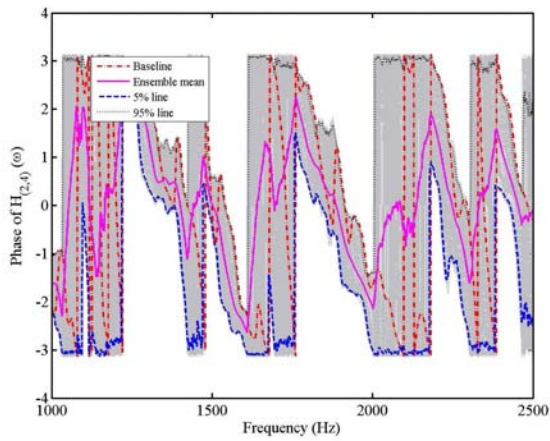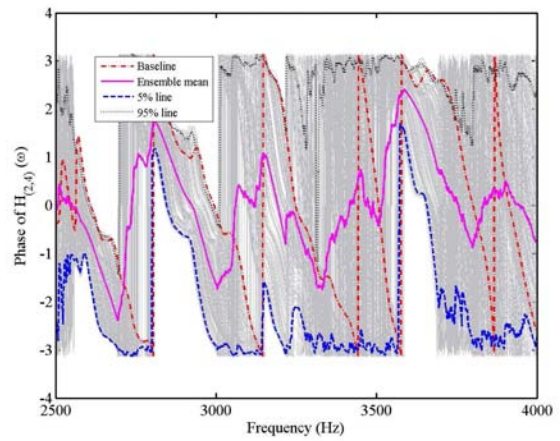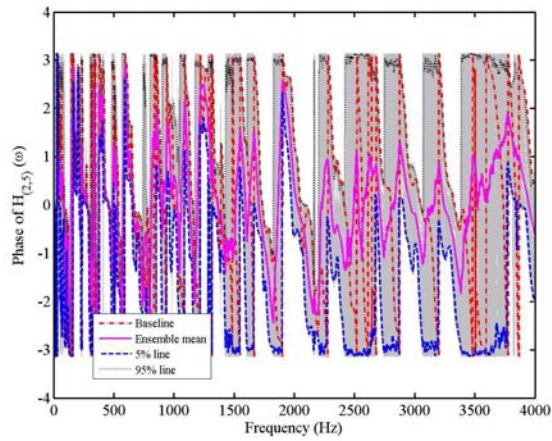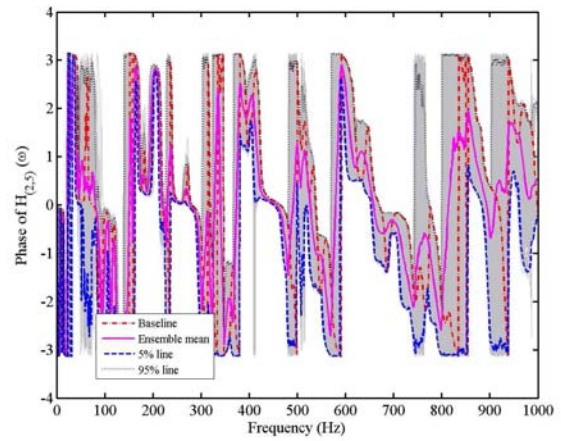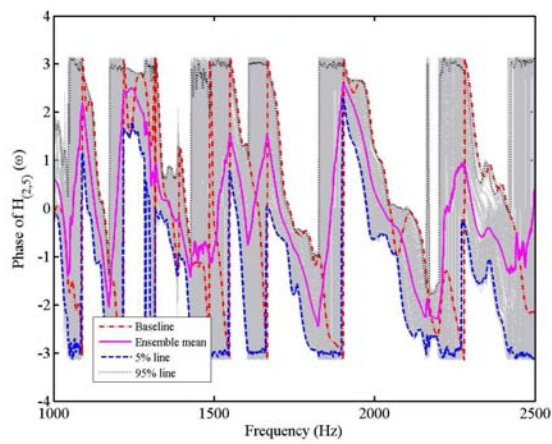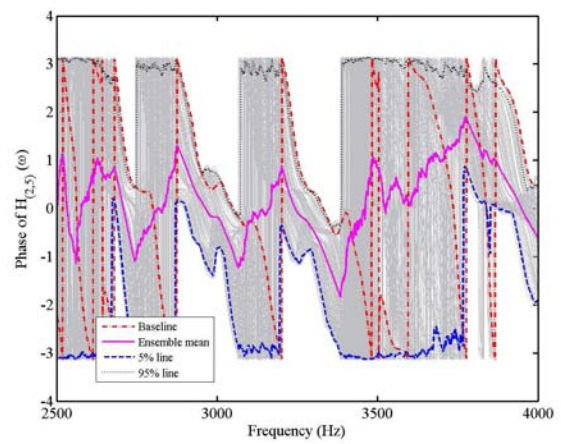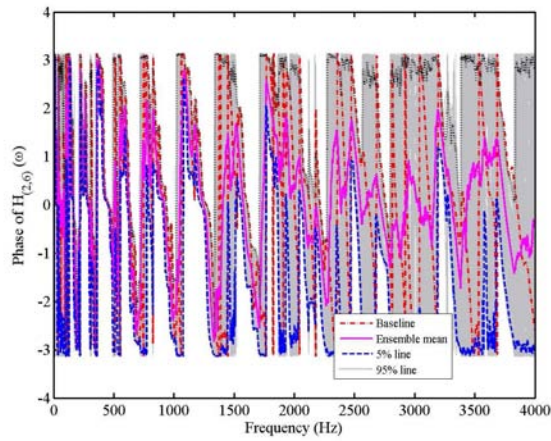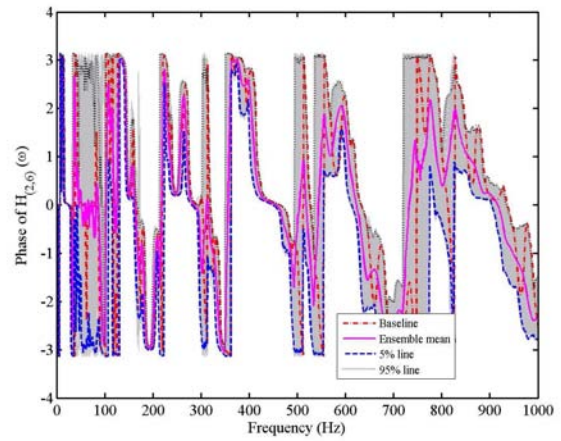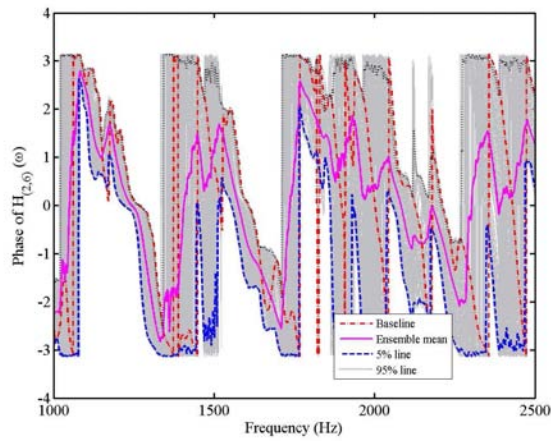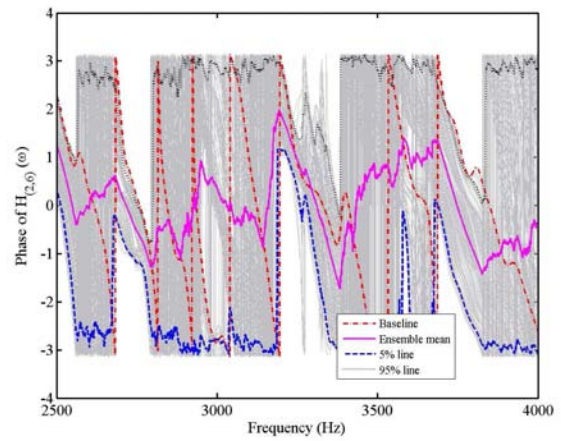
(b) Low-frequency response

(c) Medium-frequency response

(d) High-frequency response

Fig. 24. Numerically calculated amplitude of the cross-FRF of the plate at point 2 (nodal coordinate: (6,11)) with 10 randomly placed oscillators. 100 FRFs, together with the ensemble mean, 5% and 95% probability points are shown.

(a) Response across the frequency range

(b) Low-frequency response

(c) Medium-frequency response

(d) High-frequency response

Fig. 25. Numerically calculated amplitude of the cross-FRF of the plate at point 3 (nodal coordinate: (11,3)) with 10 randomly placed oscillators. 100 FRFs, together with the ensemble mean, 5% and 95% probability points are shown.

(a) Response across the frequency range

(b) Low-frequency response

(c) Medium-frequency response

(d) High-frequency response

Fig. 26. Numerically calculated amplitude of the cross-FRF of the plate at point 4 (nodal coordinate: (14,14)) with 10 randomly placed oscillators. 100 FRFs, together with the ensemble mean, 5% and 95% probability points are shown.

(a) Response across the frequency range

(b) Low-frequency response

(c) Medium-frequency response

(d) High-frequency response

Fig. 27. Numerically calculated amplitude of the cross-FRF of the plate at point 5 (nodal coordinate: (18,2)) with 10 randomly placed oscillators. 100 FRFs, together with the ensemble mean, 5% and 95% probability points are shown.
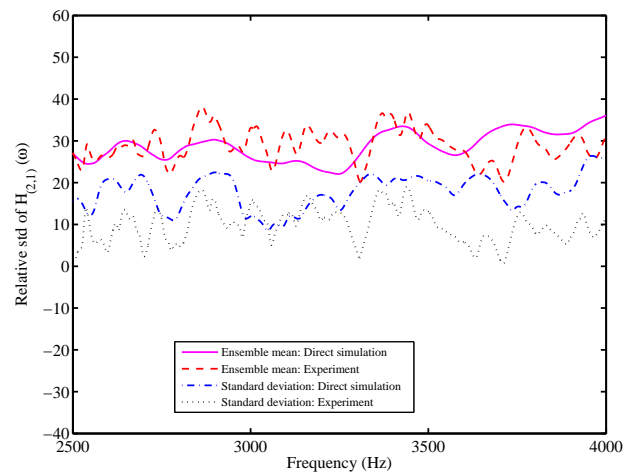
(a) Response across the frequency range

(b) Low-frequency response

(c) Medium-frequency response

(d) High-frequency response

Fig. 28. Numerically calculated amplitude of the cross-FRF of the plate at point 6 (nodal coordinate: (21,10)) with 10 randomly placed oscillators. 100 FRFs, together with the ensemble mean, 5% and 95% probability points are shown.

(a) Response across the frequency range
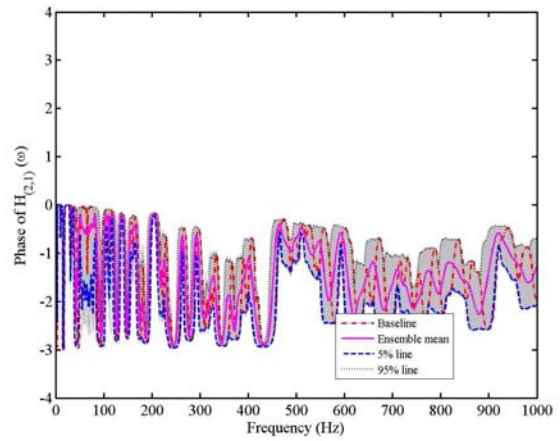
(b) Low-frequency response
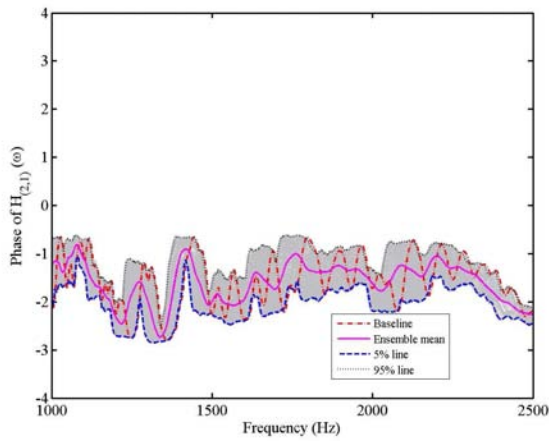
(c) Medium-frequency response
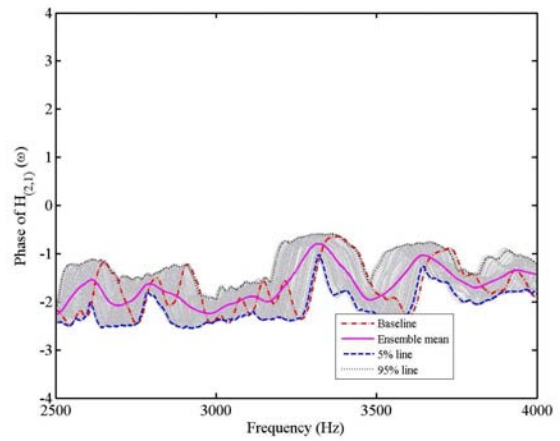
(d) High-frequency response

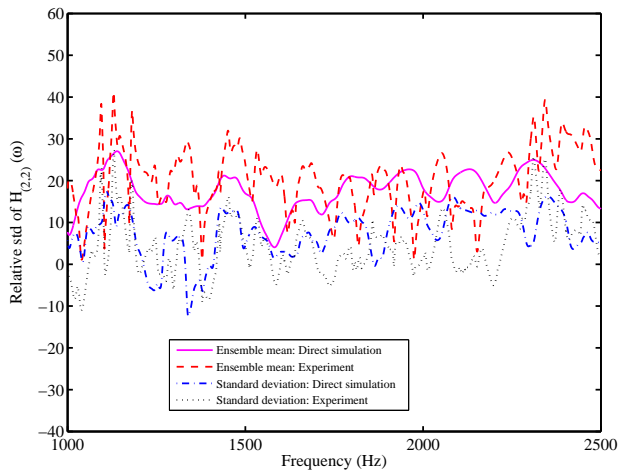Fig. 29. Numerically calculated phase of the driving-point FRF of the plate at point 1 (nodal coordinate: (4,6)) with 10 randomly placed oscillators. 100 FRFs, together with the ensemble mean, 5% and 95% probability points are shown.
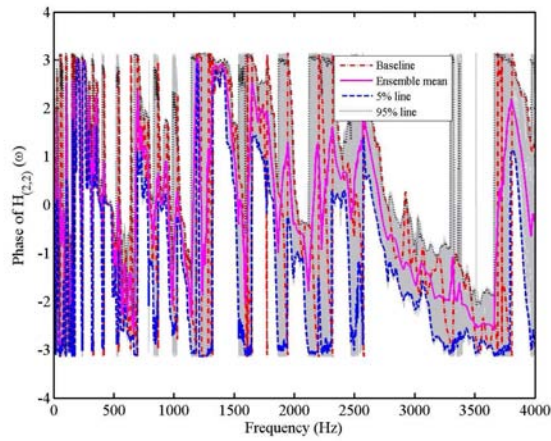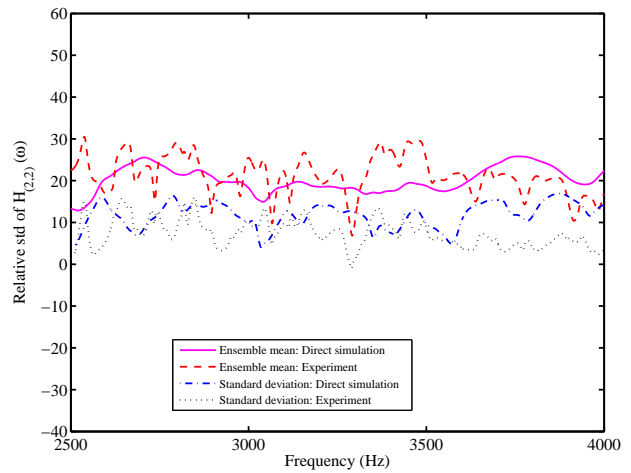
(a) Response across the frequency range
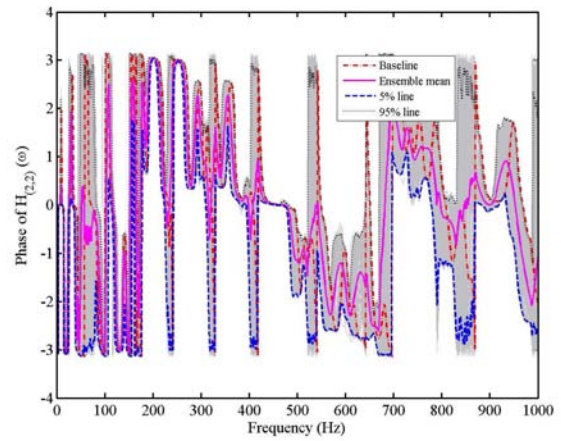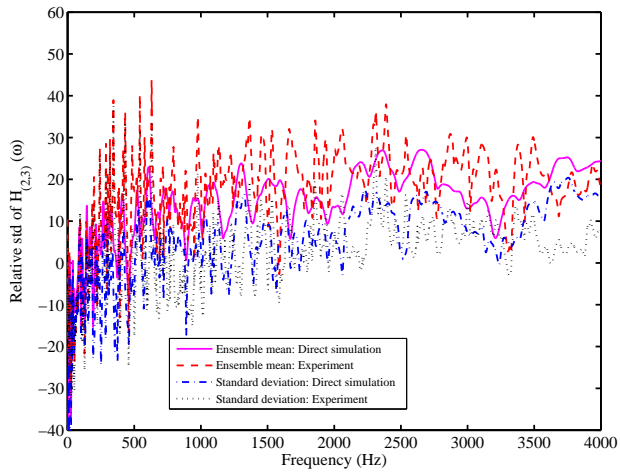
(b) Low-frequency response
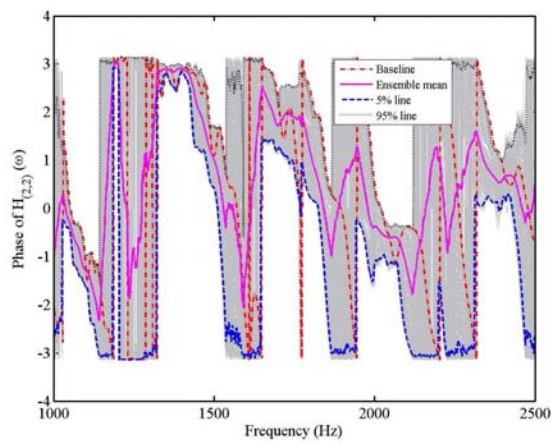
(c) Medium-frequency response

(d) High-frequency response

Fig. 30. Numerically calculated phase of the cross-FRF of the plate at point 2 (nodal coordinate: (6,11)) with 10 randomly placed oscillators. 100 FRFs, together with the ensemble mean, 5% and 95% probability points are shown.

(a) Response across the frequency range

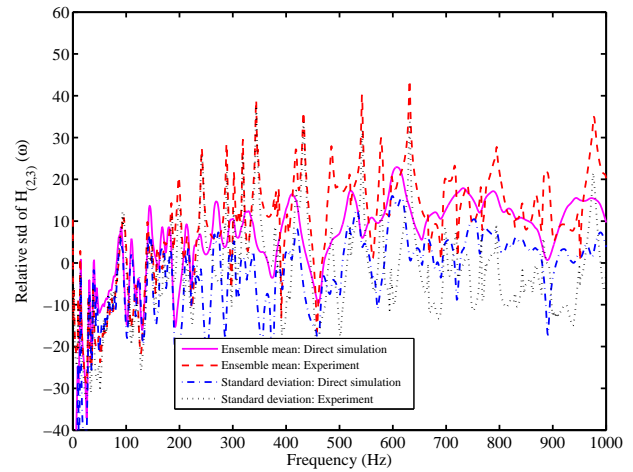(b) Low-frequency response

(c) Medium-frequency response

(d) High-frequency response

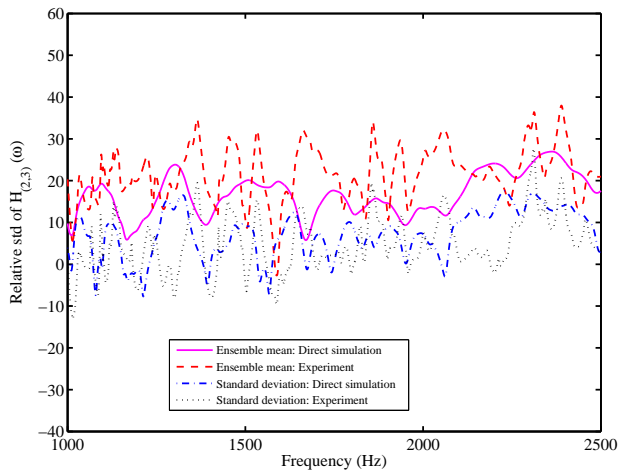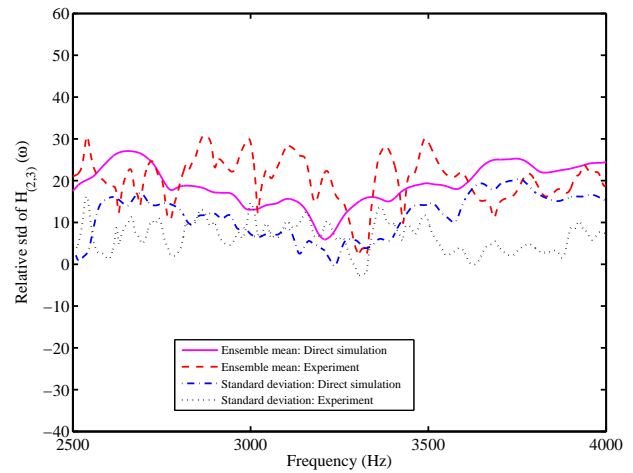Fig. 31. Numerically calculated phase of the cross-FRF of the plate at point 3 (nodal coordinate: (11,3)) with 10 randomly placed oscillators. 100 FRFs, together with the ensemble mean, 5% and 95% probability points are shown.

(a) Response across the frequency range
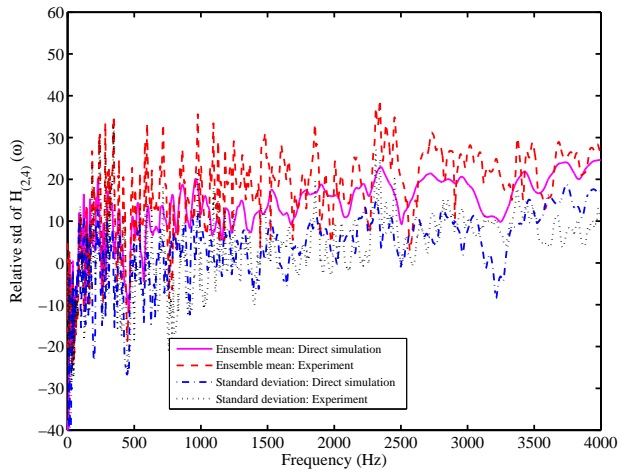
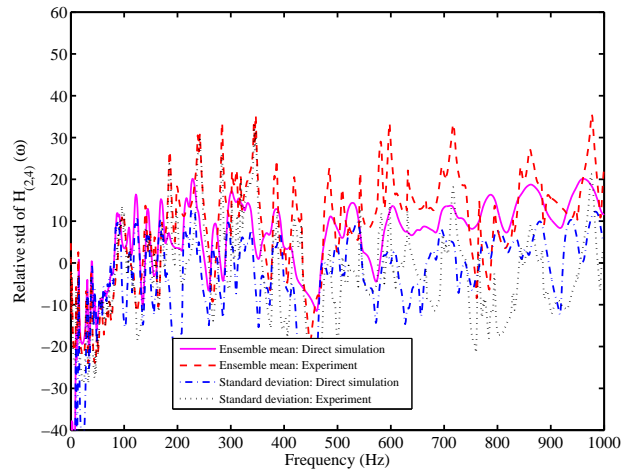(b) Low-frequency response

(c) Medium-frequency response

(d) High-frequency response

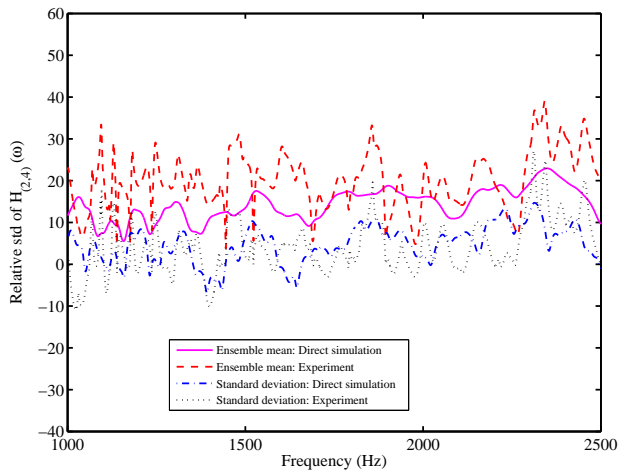Fig. 32. Numerically calculated phase of the cross-FRF of the plate at point 4 (nodal coordinate: (14,14)) with 10 randomly placed oscillators. 100 FRFs, together with the ensemble mean, 5% and 95% probability points are shown.
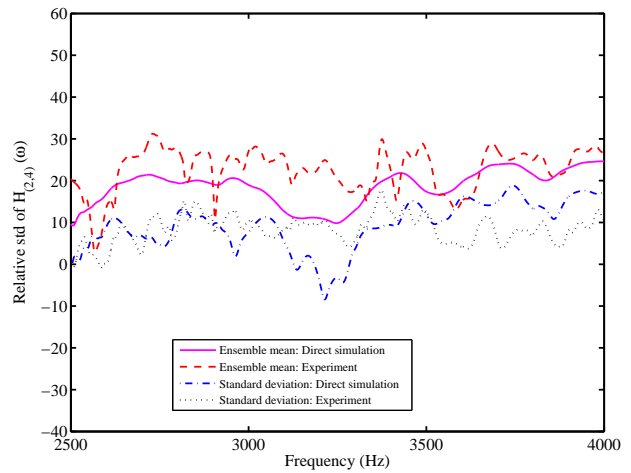
(a) Response across the frequency range

(b) Low-frequency response

(c) Medium-frequency response

(d) High-frequency response

Fig. 33. Numerically calculated phase of the cross-FRF of the plate at point 5 (nodal coordinate: (18,2)) with 10 randomly placed oscillators. 100 FRFs, together with the ensemble mean, 5% and 95% probability points are shown.

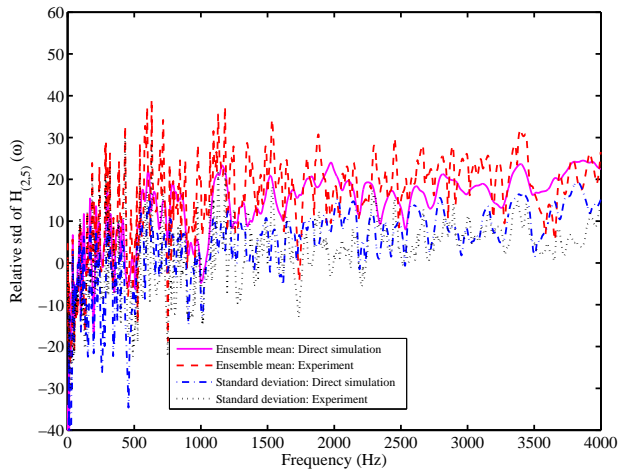(a) Response across the frequency range

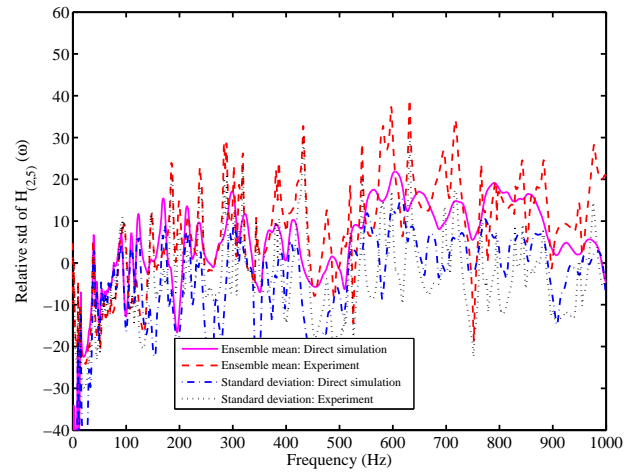(b) Low-frequency response

(c) Medium-frequency response

(d) High-frequency response

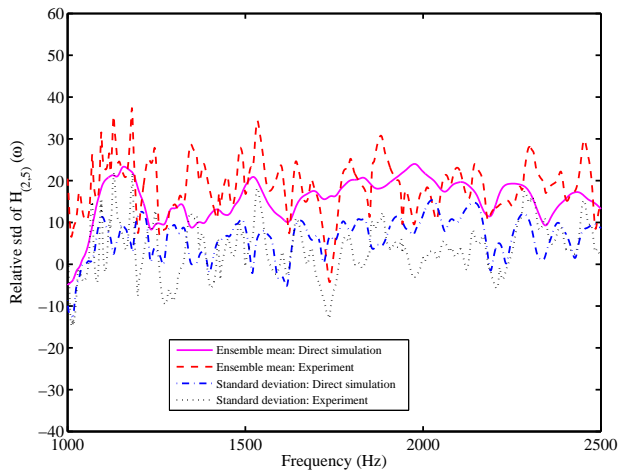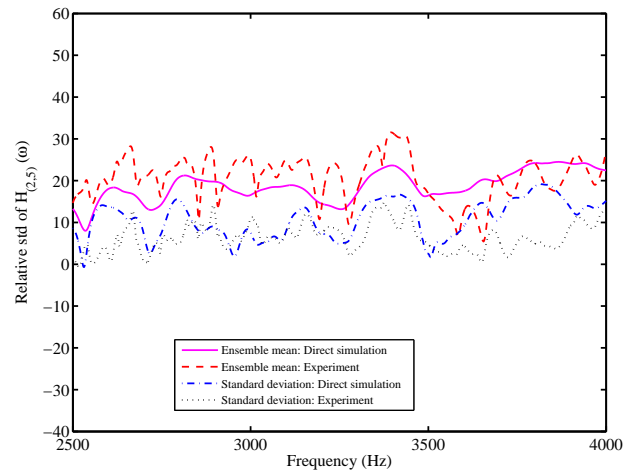Fig. 34. Numerically calculated phase of the cross-FRF of the plate at point 6 (nodal coordinate: (21,10)) with 10 randomly placed oscillators. 100 FRFs, together with the ensemble mean, 5% and 95% probability points are shown.

higher compared to the phase of the driving-point FRF. Overall, the numerical results show reasonably similar trend to the experiential results.

6 Comparisons between numerical and experimental results

6.1 Amplitude spectra

It is useful to compare the experimental results with the Monte Carlo simulation results. Figure 35 compares the ensemble mean and standard deviation of the amplitude of the driving-point frequency response function (FRF) at point 1 obtained from the experiment and Monte Carlo simulation. Figures 35(b)-(d) show the low, medium and high-frequency response separately, obtained by zooming around the appropriate frequency ranges in Figure 35(a). To the best of the authors knowledge, this is perhaps the first time where direct comparison between experimental and analytical (simulation) results for stochastic dynamical systems have been reported. The standard deviation of the amplitude of the FRF reaches a peak at the system natural frequencies, which is also predicted by the numerical simulation. Qualitatively the simulation results agree well with the experimental results. The main reason for the discrepancies, especially in the low frequency regions, is probably due to the incorrect value of the damping factors. In the simulation study a constant damping factor of 0.7% is assumed for all of the modes. Ideally one should measure modal damping factors from experimental measurements for all of the samples and for as many modes as possible and perhaps take an average across the samples for every mode. quivalent comparisons for point 2 (a cross FRF) are shown in Figure 36. For both points, the experimental mean and standard deviation in the low frequency range is quite high compared to numerical results. This can again be attributed to the wrong values of modal damping factors in the analytical model since the pattern of the peaks are strikingly similar but they are separated in 'height'. This is a clear indication that the damping values are incorrect in the simulation model. Therefore, one of the key outcomes of this experimental study is that wrong values of the modal damping factors can lead to significant errors in the response variance prediction even if everything else is performed correctly.

6.2 Phase spectra

Figure 41 compares the ensemble mean and standard deviation of the phase of the driving-point frequency response function at point 1 obtained from the experiment and Monte Carlo simulation. Figures 41(b)-(d) show the low, medium and high-frequency response separately, obtained by zooming around the appropriate frequency ranges in Figure 41(a). Except in
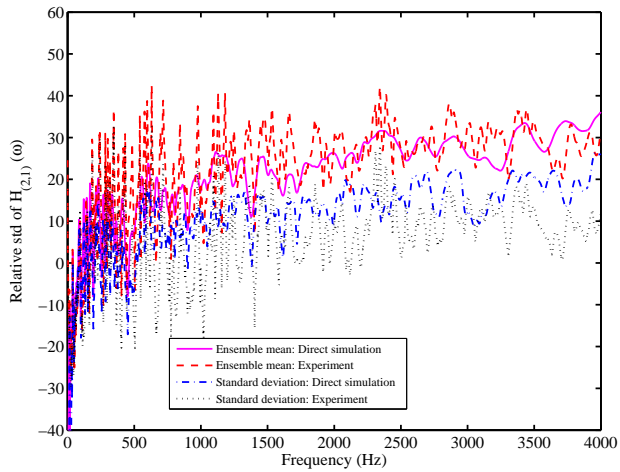
(a) Response across the frequency range
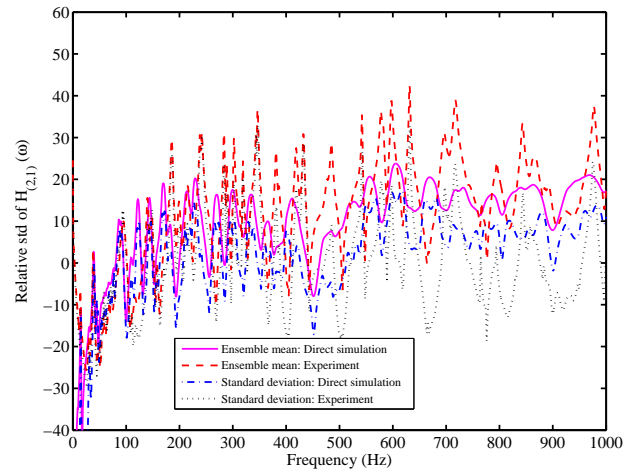
(b) Low-frequency response
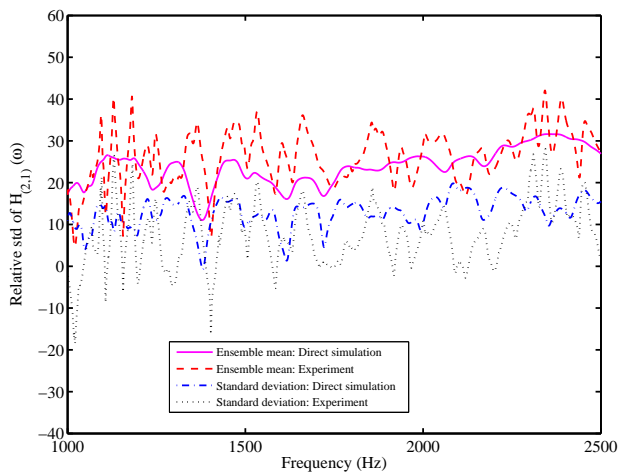
(c) Medium-frequency response

(d) High-frequency response

Fig. 35. Comparison of the mean and standard deviation of the amplitude of the driving-point FRF of the plate at point 1 (nodal coordinate: (4,6)) with 10 randomly placed oscillators. 100 FRFs, together with the ensemble mean, 5% and 95% probability points are shown.
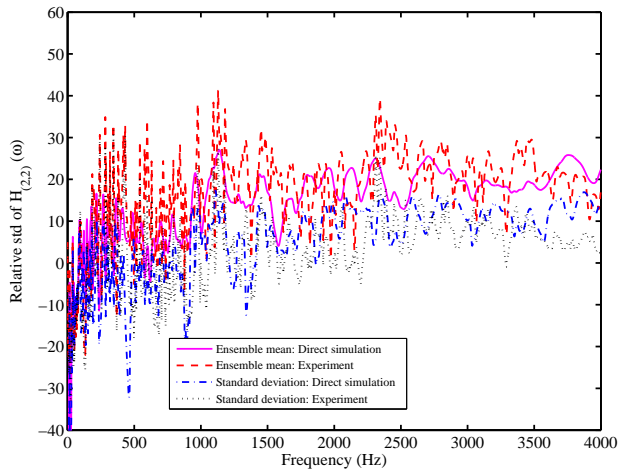
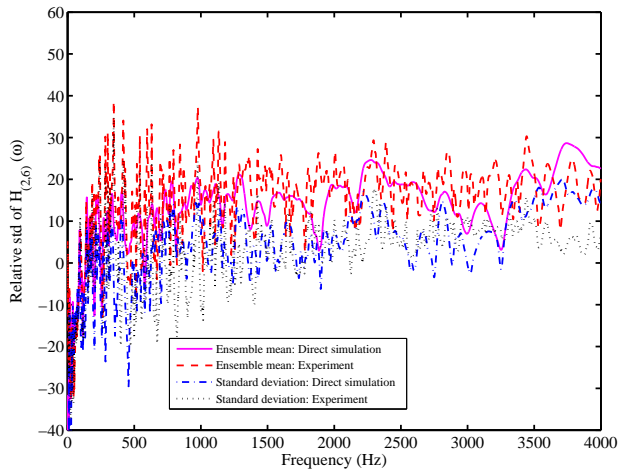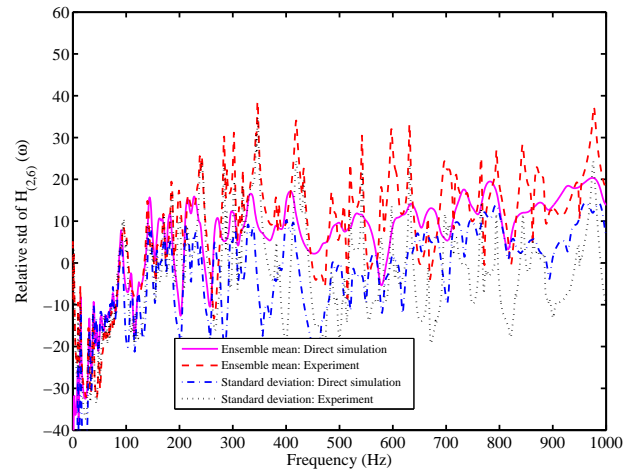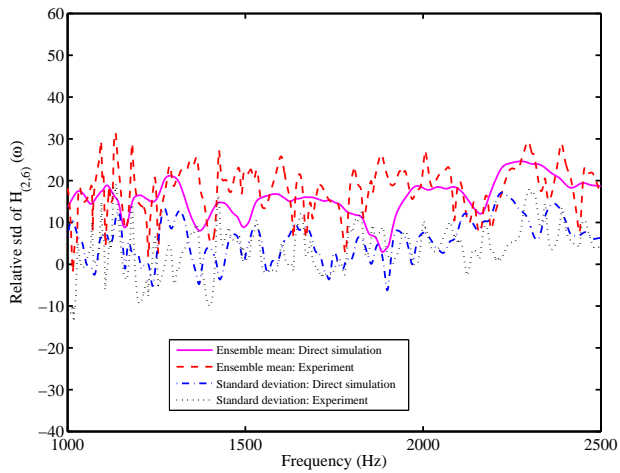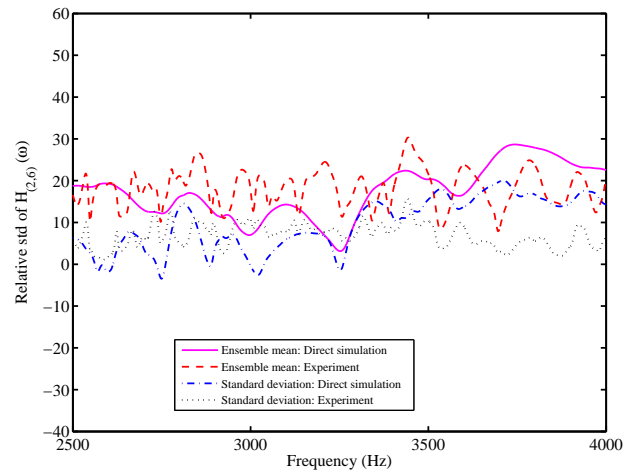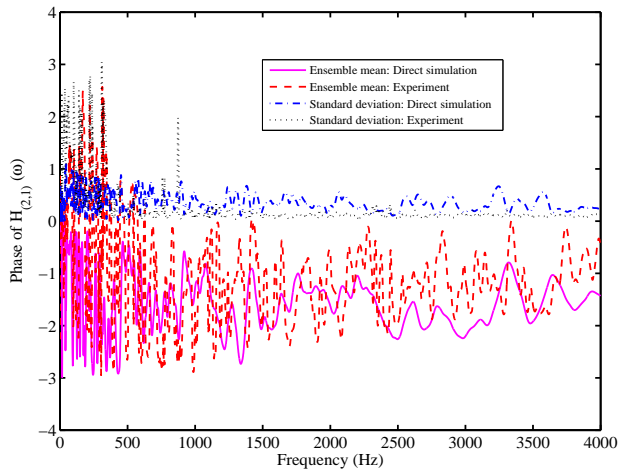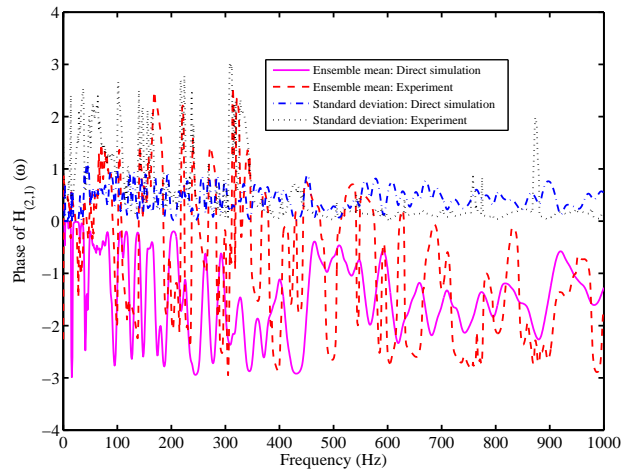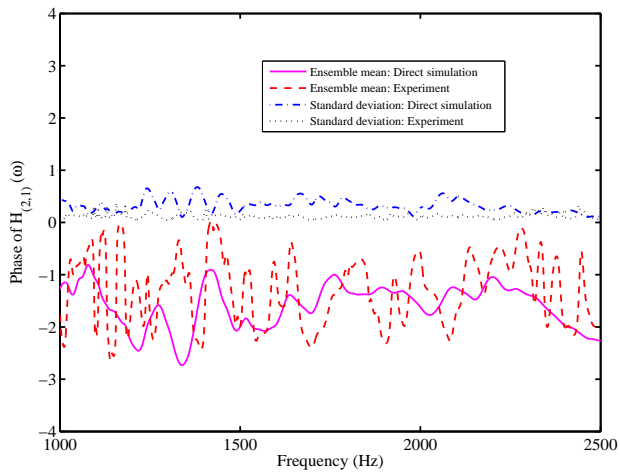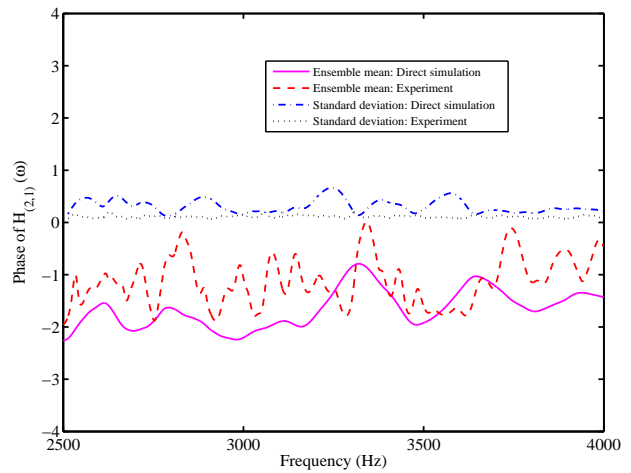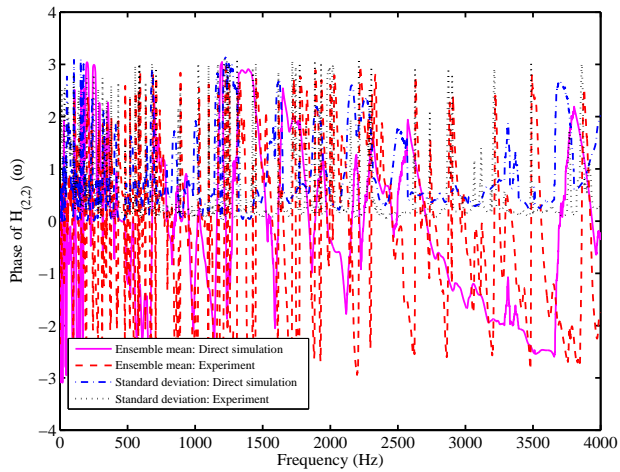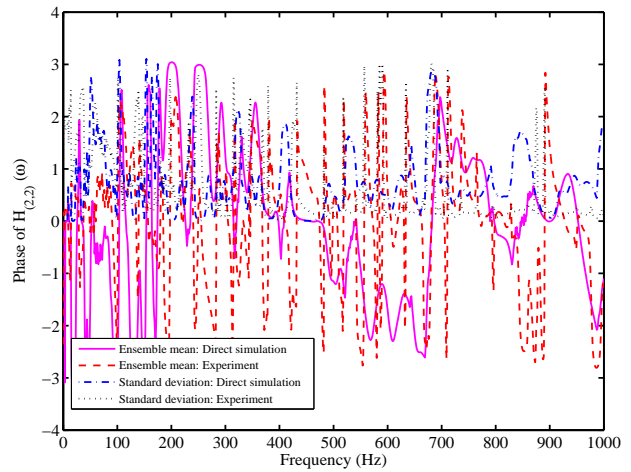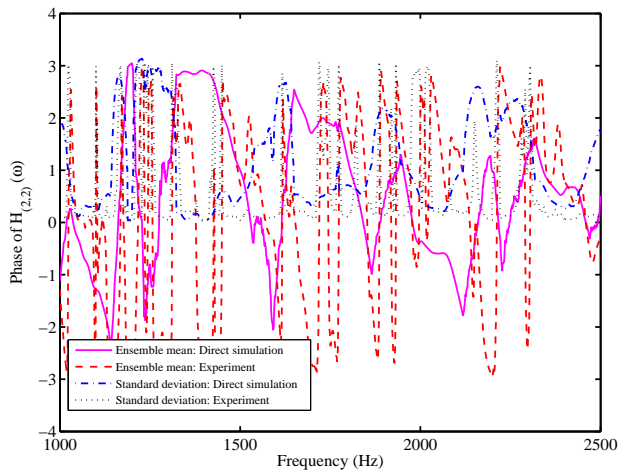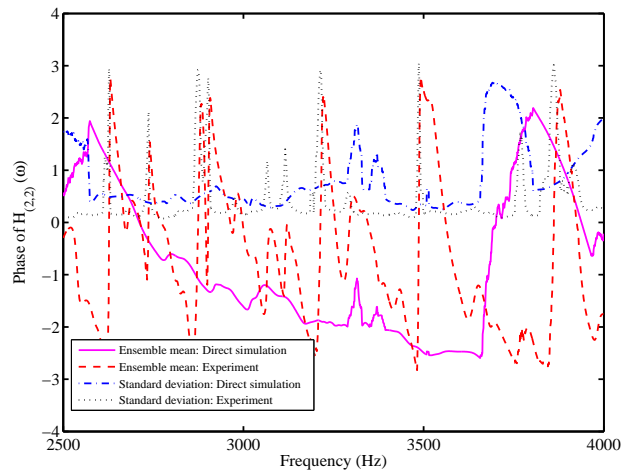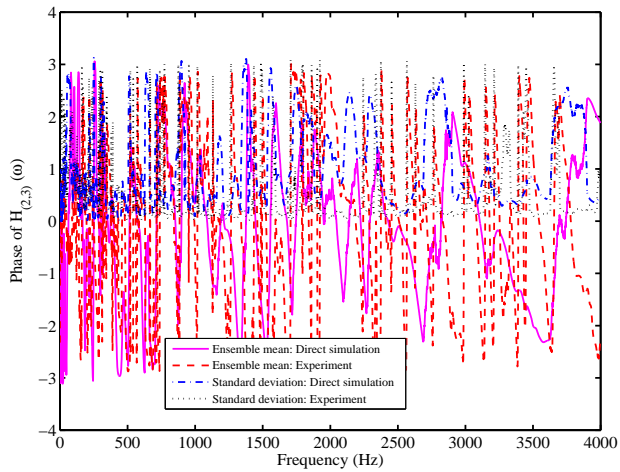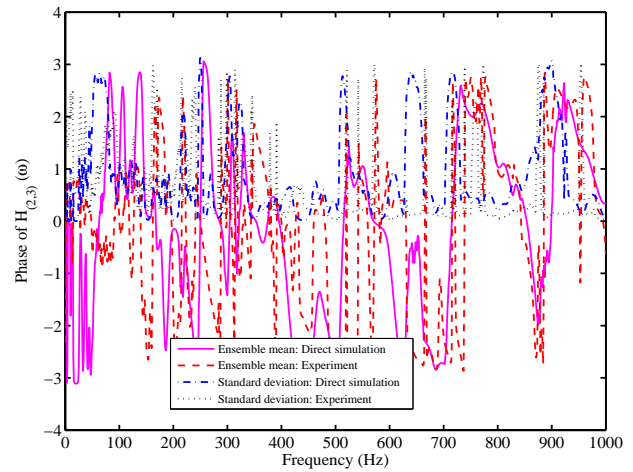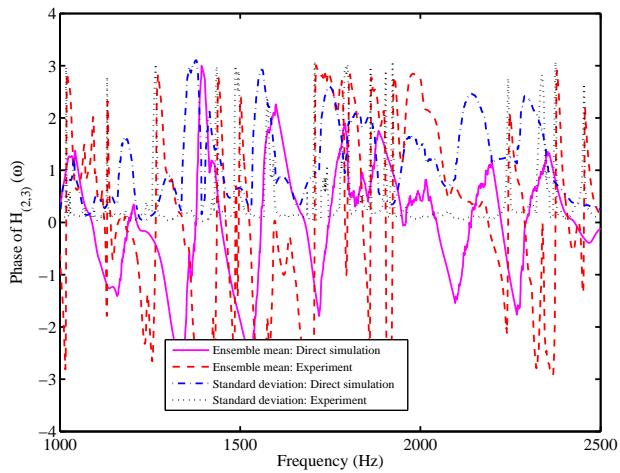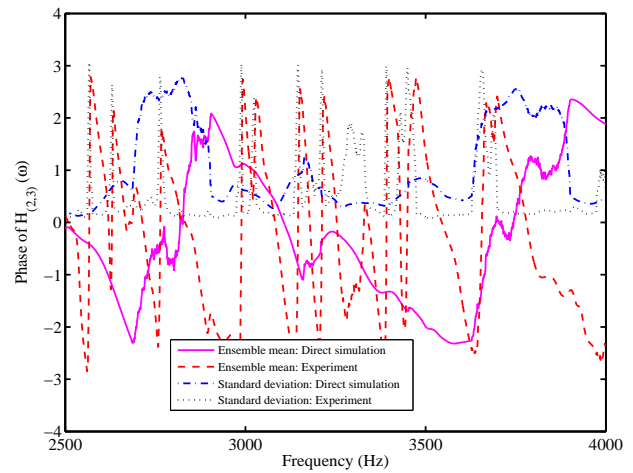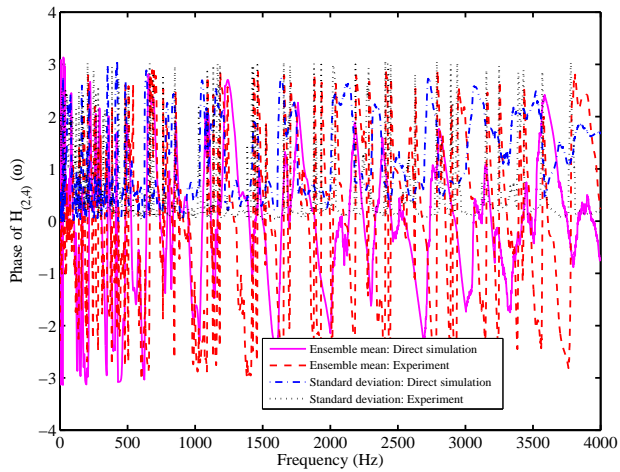(a) Response across the frequency range
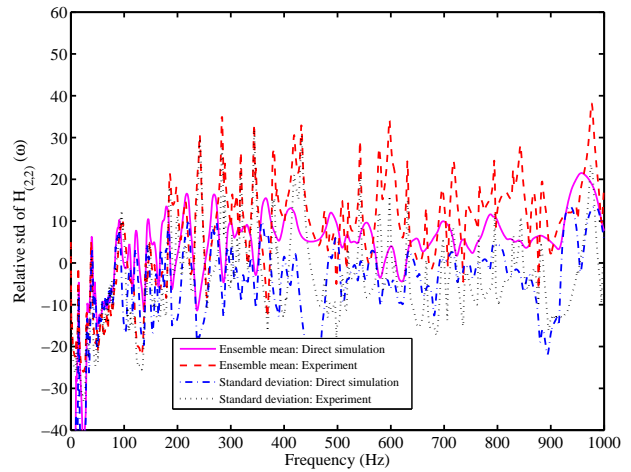
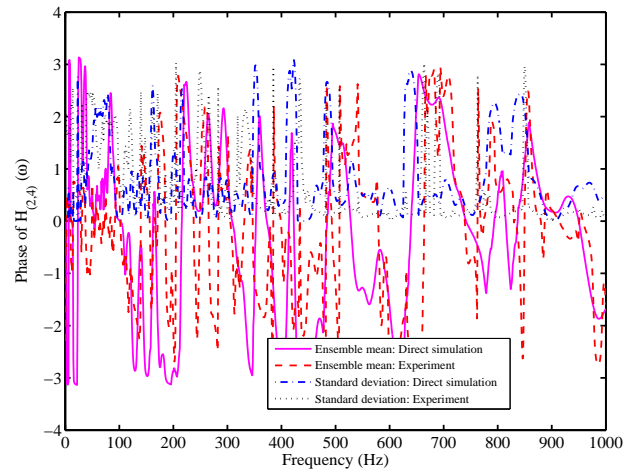(b) Low-frequency response

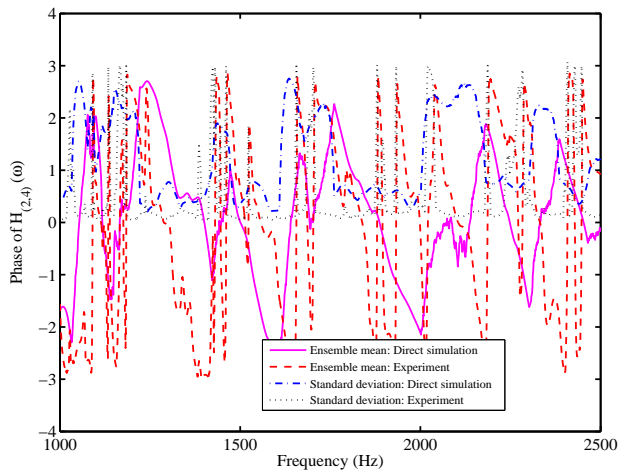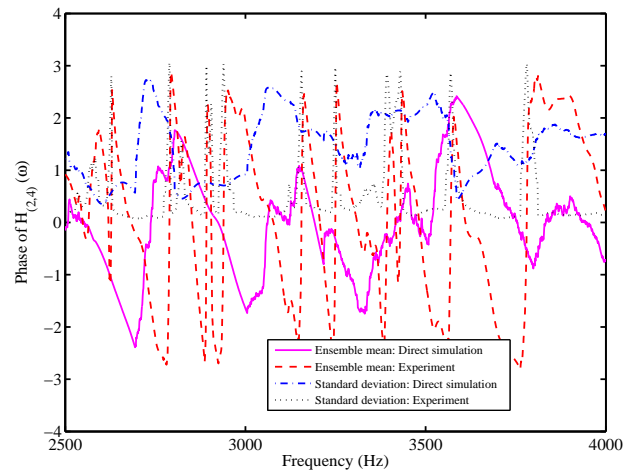(c) Medium-frequency response

(d) High-frequency response

Fig. 36. Comparison of the mean and standard deviation of the amplitude of the cross-FRF of the plate at point 2 (nodal coordinate: (6,11)) with 10 randomly placed oscillators. 100 FRFs, together with the ensemble mean, 5% and 95% probability points are shown.

(a) Response across the frequency range
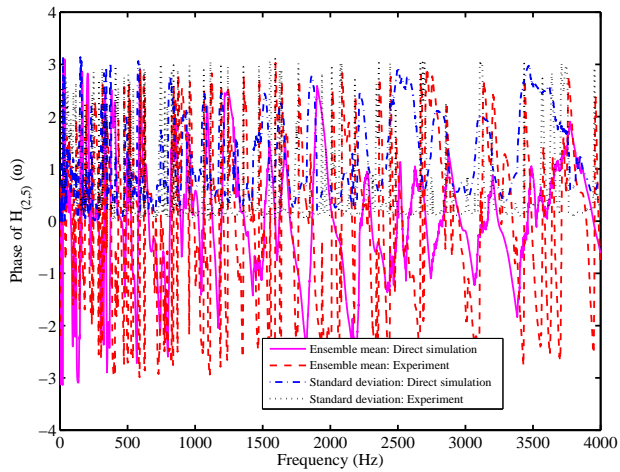
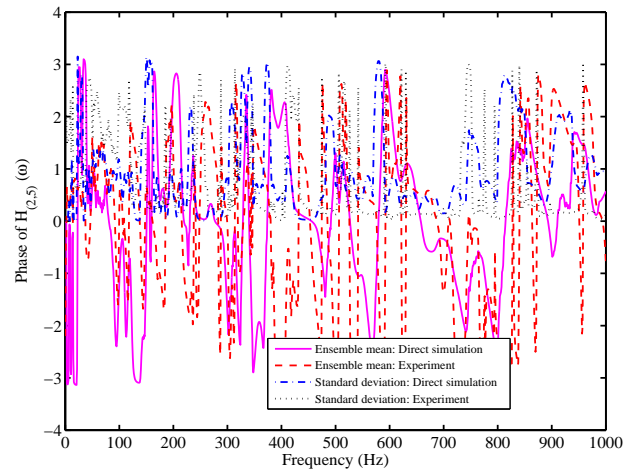(b) Low-frequency response

(c) Medium-frequency response

(d) High-frequency response

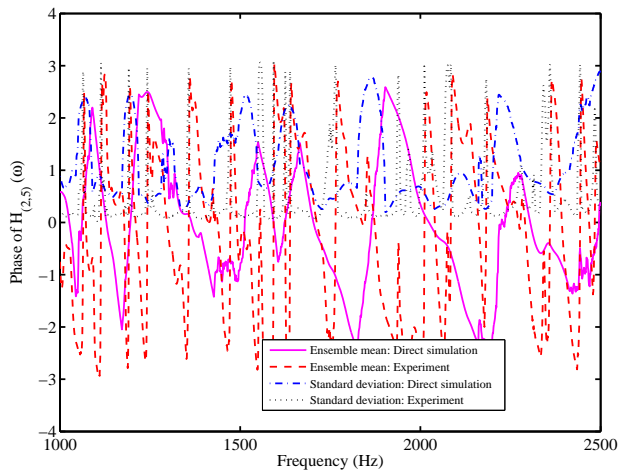Fig. 37. Comparison of the mean and standard deviation of the amplitude of the cross-FRF of the plate at point 3 (nodal coordinate: (11,3)) with 10 randomly placed oscillators. 100 FRFs, together with the ensemble mean, 5% and 95% probability points are shown.
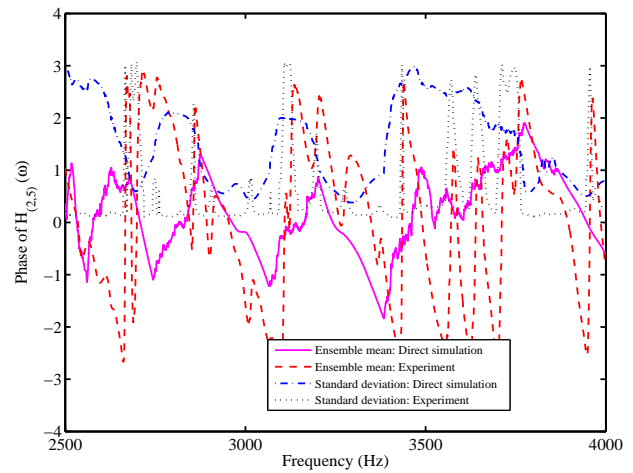
(a) Response across the frequency range
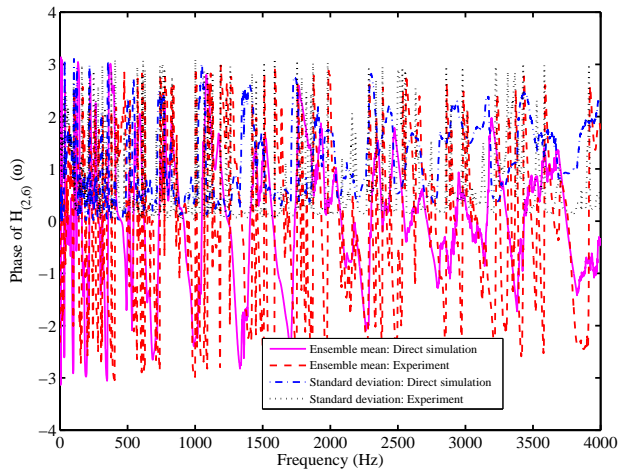
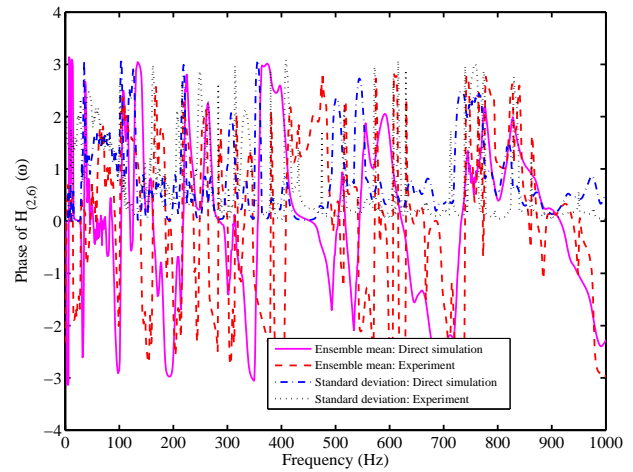(b) Low-frequency response

(c) Medium-frequency response

(d) High-frequency response

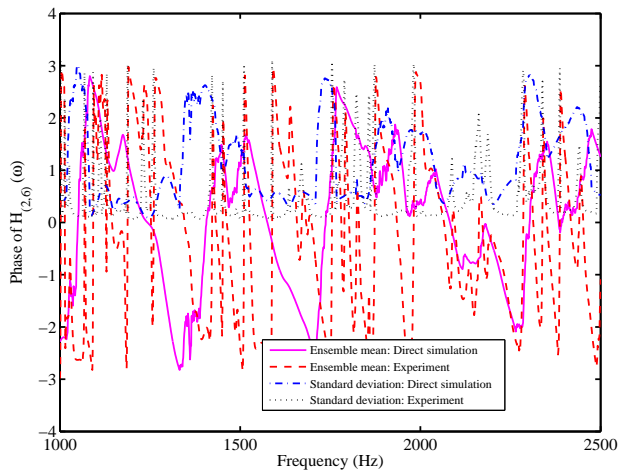Fig. 38. Comparison of the mean and standard deviation of the amplitude of the cross-FRF of the plate at point 4 (nodal coordinate: (14,14)) with 10 randomly placed oscillators. 100 FRFs, together with the ensemble mean, 5% and 95% probability points are shown.

(a) Response across the frequency range

(b) Low-frequency response

(c) Medium-frequency response

(d) High-frequency response

Fig. 39. Comparison of the mean and standard deviation of the amplitude of the cross-FRF of the plate at point 5 (nodal coordinate: (18,2)) with 10 randomly placed oscillators. 100 FRFs, together with the ensemble mean, 5% and 95% probability points are shown.
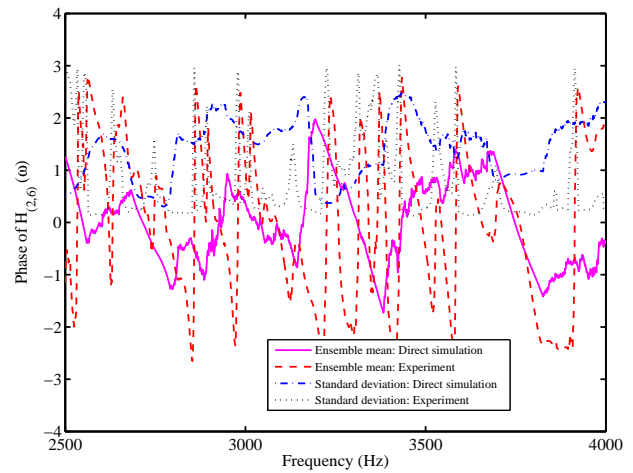
(a) Response across the frequency range

(b) Low-frequency response

(c) Medium-frequency response

(d) High-frequency response

Fig. 40. Comparison of the mean and standard deviation of the amplitude of the cross-FRF of the plate at point 6 (nodal coordinate: (21,10)) with 10 randomly placed oscillators. 100 FRFs, together with the ensemble mean, 5% and 95% probability points are shown.

(a) Response across the frequency range

(b) Low-frequency response

(c) Medium-frequency response

(d) High-frequency response

Fig. 41. Comparison of the mean and standard deviation of the phase of the driving-point FRF of the plate at point 1 (nodal coordinate: (4,6)) with 10 randomly placed oscillators. 100 FRFs, together with the ensemble mean, 5% and 95% probability points are shown.

(a) Response across the frequency range

(b) Low-frequency response

(c) Medium-frequency response

(d) High-frequency response

Fig. 42. Comparison of the mean and standard deviation of the phase of the cross-FRF of the plate at point 2 (nodal coordinate: (6,11)) with 10 randomly placed oscillators. 100 FRFs, together with the ensemble mean, 5% and 95% probability points are shown.

(a) Response across the frequency range

(b) Low-frequency response

(c) Medium-frequency response

(d) High-frequency response

Fig. 43. Comparison of the mean and standard deviation of the phase of the cross-FRF of the plate at point 3 (nodal coordinate: (11,3)) with 10 randomly placed oscillators. 100 FRFs, together with the ensemble mean, 5% and 95% probability points are shown.

(a) Response across the frequency range

(b) Low-frequency response

(c) Medium-frequency response

(d) High-frequency response

Fig. 44. Comparison of the mean and standard deviation of the phase of the FRF of the plate at point 4 (nodal coordinate: (14,14)) with 10 randomly placed oscillators. 100 FRFs, together with the ensemble mean, 5% and 95% probability points are shown.

(a) Response across the frequency range

(b) Low-frequency response

(c) Medium-frequency response

(d) High-frequency response

Fig. 45. Comparison of the mean and standard deviation of the phase of the FRF of the plate at point 5 (nodal coordinate: (18,2)) with 10 randomly placed oscillators. 100 FRFs, together with the ensemble mean, 5% and 95% probability points are shown.

(a) Response across the frequency range

(b) Low-frequency response

(c) Medium-frequency response

(d) High-frequency response

Fig. 46. Comparison of the mean and standard deviation of the phase of the FRF of the plate at point 6 (nodal coordinate: (21,10)) with 10 randomly placed oscillators. 100 FRFs, together with the ensemble mean, 5% and 95% probability points are shown.

the low frequency range, the standard deviation of the phase of the FRF is very small and the experimental and simulation results agree well. The patterns of the mean results from the experiment and simulation is very similar. The discrepancy is again primarily due to the incorrect damping model in the numerical results. quivalent comparisons for point 2 (a cross FRF) are shown in Figure 42. The experimental mean in the mid and high frequency range is quite different compared to the numerical results. This is perhaps again due to the wrong damping model and it is well known that damping has significant affect on the phase of the frequency response functions.

7 Conclusions

An experiment on a cantilever plate that may be used to study methods to quantify uncertainty in the dynamics of structures is described. The system is easy to model and the results of an one hundred sample experiment with randomly placed oscillators are described in this paper. The randomly located oscillators with randomly varying stiffness is designed to simulate model uncertainty. Test results from one hundred nominally identical systems are presented. Special measures have been taken so that the uncertainty in the response only arises from the randomness in the oscillator locations and the experiments are repeatable with minimum changes. Such novel measures include (a) the use of a shaker as an impact hammer to ensure a consistent force and location for all of the 101 tests, (b) the use of a hard steel tip to obtain relatively noise-free data up to 4 KHz, (c) the employment of a grid system and nodal points to minimize the error in measuring the oscillator and hammer locations, and (d) the use of magnets to attach the oscillators. The statistics of the frequency response function are measured at six points (only two are shown in the paper, but others can be obtained from the uploaded data files) on the plate for low, medium and high frequency ranges. There is more variability in the FRF at the low frequency range compared to the high frequency range. This is because of the fact that the natural frequencies of the randomly placed oscillators are quite low. The experimental results are directly compared with numerical Monte Carlo simulation. A finite element model with simple thin plate elements is used in the analytical work. The pattern of the response mean and standard deviation obtained in the experimental analysis is predicted. This is perhaps the first time where such a direct comparison between experimental and analytical (simulation) results for a stochastic dynamical system with model uncertainty have been reported in stochastic mechanics literature. The discrepancies between the two approaches are attributed to incorrect values for damping used in the numerical model.

This data may be used for the model validation and uncertainty quantification of dynamical systems with nonparametric uncertainty. Of course one hundred samples are not enough for a

reliable statistical analysis. But to the best of the authors knowledge, this is perhaps the most comprehensive set of experimentally measured response data available for dynamical systems with model uncertainty to date.

Acknowledgements

References

[1]   Adhikari S, Friswell MI, Lonkar K. Experimental case studies for uncertainty quantification in structural dynamics: Part 1, beam experiment. Probabilistic Engineering Mechanics 2007;Under review.

[2]   Shinozuka M, Yamazaki F. Stochastic finite element analysis: an introduction. In *Stochastic structural dynamics: Progress in theory and applications*, Ariaratnam ST, Schueller GI, Elishakoff I, editors. London: Elsevier Applied Science 1998; .

[3]   Ghanem R, Spanos P. *Stochastic Finite Elements: A Spectral Approach*. New York, USA: Springer-Verlag 1991.

[4]   Kleiber M, Hien TD. *The Stochastic Finite Element Method*. Chichester: John Wiley 1992.

[5]   Manohar CS, Adhikari S. Dynamic stiffness of randomly parametered beams. Probabilistic Engineering Mechanics 1998;13(1):39–51.

[6]   Adhikari S, Manohar CS. Dynamic analysis of framed structures with statistical uncertainties. International Journal for Numerical Methods in Engineering 1999;44(8):1157–1178.

[7]   Adhikari S, Manohar CS. Transient dynamics of stochastically parametered beams. ASCE Journal of Engineering Mechanics 2000;126(11):1131–1140.

[8] Haldar A, Mahadevan S. *Reliability Assessment Using Stochastic Finite Element Analysis*. New York, USA: John Wiley and Sons 2000.

[9] Sudret B, Der-Kiureghian A. Stochastic Finite Element Methods and Reliability. Tech. Rep. UCB/SEMM-2000/08, Department of Civil & Environmental Engineering, University Of California, Berkeley 2000.

[10] Elishakoff I, Ren YJ. *Large Variation Finite Element Method for Stochastic Problems*. Oxford, U.K.: Oxford University Press 2003.

[11] Hanson KM, Hemez FM. A framework for assessing confidence in computational predictions - Computational validation series: Part 3. Experimental Techniques 2001;25(4):50–55.

[12] Oberkampf WL, Trucano TG. Verification and validation in computational fluid dynamics. Progress in Aerospace Sciences 2002;38(3):209–272.

[13] Oberkampf WL, DeLand SM, Rutherford BM, Diegert KV, Alvin KF. Error and uncertainty in modeling and simulation. Reliability Engineering System Safety 2002;75(3):333–357.

[14] Hemez FM. Overview of Uncertainty Quantification and Model Verification and Validation. In *Pan American Advanced Study Institute (PASI) on Damage Prognosis*. Florianopolis, Brazil 2003; .

[15] Hemez FM. Uncertainty Quantification and the Verification and Validation of Computational Models. In *Damage Prognosis for Aerospace, Civil and Mechanical Systems*, Inman DJ, Farrar CR, Jr. VL, , Jr. VS, editors. London, United Kingdom: John Wiley & Sons Ltd. 2004; .

[16] Ferson S, Joslyn CA, Helton JC, Oberkampf WL, Sentz K. Summary from the epistemic uncertainty workshop: consensus amid diversity. Reliability Engineering System Safety 2004;85(1-3):355–369.

[17] Oberkampf WL, Trucano TG, Hirsch C. Verification, validation, and predictive capability in computational engineering and physics. Applied Mechanics Reviews ASME 2004; 57(5):345–384.

[18] Oberkampf WL, Barone MF. Measures of agreement between computation and experi-

ment: Validation metrics. Journal of Computational Physics 2006;217(1):5–36.

[19] Trucano TG, Swiler LP, Igusa T, Oberkampf WL, Pilch M. Calibration, validation, and sensitivity analysis: What's what. Reliability Engineering System Safety 2006;91(10-11):1331–1357.

[20] Adhikari S, Sarkar A. The nature of epistemic uncertainty in linear dynamical systems. In *Proceedings of the 25th International Modal Analysis Conference (IMAC-XXV)*. Orlando, Florida, USA 2007; .

[21] Kompella MS, Bernhard BJ. Measurement of the statistical variations of structural-acoustics characteristics of automotive vehicles. In *SAE Noise and Vibration Conference*. Warrendale, USA: Society of Automotive Engineers 1993; .

[22] Fahy F. *Foundations of Engineering Acoustics*. London, UK: Academic Press Inc., 2000.

[23] Friswell MI, Coote JA, Terrell MJ, Adhikari S, Fonseca JR, Lieven NAJ. Experimental Data for Uncertainty Quantification. In *Proceedings of the 23rd International Modal Analysis Conference (IMAC - XXIII)*. Orlando, Florida, USA: Society of Experimental Mechanics (SEM) 2005; .

[24] Ewins DJ. *Modal Testing: Theory and Practice*. Baldock, England: Research Studies Press, second edn. 2000.

[25] Maia NMM, Silva JMM, editors. *Theoretical and Experimental Modal Analysis*. Engineering Dynamics Series. Taunton, England: Research Studies Press 1997. Series Editor, J. B. Robetrs.

[26] Silva JMME, Maia NMM, editors. *Modal Analysis and Testing: Proceedings of the NATO Advanced Study Institute*, NATO Science Series: E: Applied Science. Sesimbra, Portugal 1998.

List of Figures

List of Tables